PHYSICAL REVIEW D **91,** 114505 (2015)

Neutral B meson mixings and B meson decay constants with static heavy and domain-wall light quarks

Yasumichi Aoki,[1] Tomomi Ishikawa,[2] Taku Izubuchi,[2,3] Christoph Lehner,[3] and Amarjit Soni[3]
[1]*Kobayashi-Maskawa Institute for the Origin of Particle and the Universe (KMI), Nagoya University, Nagoya 464-8602, Japan*
[2]*RIKEN BNL Research Center, Brookhaven National Laboratory, Upton, New York 11973, USA*
[3]*Physics Department, Brookhaven National Laboratory, Upton, New York 11973, USA*

(Received 14 July 2014; published 12 June 2015)

Neutral B meson mixing matrix elements and B meson decay constants are calculated. The static approximation is used for the b quark and the domain-wall fermion formalism is employed for light quarks. The calculations are carried out on $2+1$-flavor dynamical ensembles generated by the RBC and UKQCD collaborations with lattice spacings of 0.086 fm ($a^{-1} \sim 2.3$ GeV) and 0.11 fm (1.7 GeV), and a fixed physical spatial volume of about $(2.7\ \mathrm{fm})^3$. In the static quark action, link smearings are used to improve the signal-to-noise ratio. We employ two kinds of link smearings, HYP1 and HYP2, and their results are combined when taking the continuum limit. For the matching between the lattice and the continuum theory, one-loop perturbative $O(a)$ improvements are made to reduce discretization errors. As the most important quantity of this work, we obtain the SU(3) breaking ratio $\xi = 1.208(60)$, where the error includes both the statistical and systematic errors. (The uncertainty from an infinite b-quark mass is not included.) We also find other neutral B meson mixing quantities, $f_B\sqrt{\hat{B}_B} = 240(22)$ MeV, $f_{B_s}\sqrt{\hat{B}_{B_s}} = 290(22)$ MeV, $\hat{B}_B = 1.17(22)$, $\hat{B}_{B_s} = 1.22(13)$, and $B_{B_s}/B_B = 1.028(74)$, and the B meson decay constants $f_B = 219(17)$ MeV, $f_{B_s} = 264(19)$ MeV, and $f_{B_s}/f_B = 1.193(41)$ in the static limit of the b quark, which do not include an infinite b-quark mass uncertainty.

DOI: 10.1103/PhysRevD.91.114505 PACS numbers: 12.38.Gc, 12.39.Hg, 14.40.Nd

I. INTRODUCTION

The Standard Model (SM) of elementary particles is consistent with all experimental data thus far. The SM, however, does not yet satisfy us because it cannot answer some of our basic questions, such as the reason why the gauge group, the constituents of particles, and the number of generations in the model are chosen as they are, the hierarchical unnaturalness in mass scales between the three generations of fermions, and so on. While the existence of the Higgs boson has been experimentally confirmed at the LHC, expected new particles have not been discovered as yet. Thus, bottom-up approaches toward physics beyond the Standard Model (BSM) is becoming more and more important. In order to address BSM, precision tests for the SM are highly meaningful. By combining theoretical predictions with experimental results, it would be possible to obtain hints for the BSM. In such an attempt, the Cabibbo-Kobayashi-Maskawa (CKM) quark mixing matrix elements [1] play a crucial role in checking the consistency of the SM.

In the SM, the transition of the neutral B (B_s) meson to its anti-meson occurs via box diagrams involving the exchange of two W bosons, and this amplitude would provide a clean determination of the matrix elements V_{td} and V_{ts} assuming that V_{tb} is known. In the SM framework, the dominant contribution to the mass difference of the neutral B meson mass eigenstates is related to the CKM matrix elements by

$$\Delta m_{B_q} = \frac{G_F^2 m_W^2}{16\pi^2 m_{B_q}} |V_{tq}^* V_{tb}|^2 S_0(x_t)\eta_B \hat{\mathcal{M}}_{B_q}, \tag{1}$$

where $q = \{d, s\}$. In Eq. (1), both the Inami-Lim function $S_0(x_t)$ ($x_t = m_t^2/m_W^2$) [2] and the QCD coefficient η_B can be calculated perturbatively. $\hat{\mathcal{M}}_{B_q}$ is a renormalization-group-invariant (RGI) $\Delta B = 2$ four-fermion operator matrix element in an effective Hamiltonian of the box diagram at the low-energy scale. The mixing matrix element $\hat{\mathcal{M}}_{B_q}$ is a highly nonperturbative quantity, and thus currently the only possible method for a precise determination is via numerical lattice QCD simulations. By taking a ratio [3] of Eq. (1) between $q = d$ and s, we obtain

$$\left|\frac{V_{td}}{V_{ts}}\right| = \xi \sqrt{\frac{\Delta m_B}{\Delta m_{B_s}} \frac{m_{B_s}}{m_B}}, \tag{2}$$

where ξ is called the SU(3)-breaking ratio

$$\xi = \frac{m_B}{m_{B_s}} \sqrt{\frac{\mathcal{M}_{B_s}}{\mathcal{M}_B}}. \tag{3}$$

The ratio constrains the apex of the CKM unitary triangle, and new quark-flavor-changing interactions from BSM would affect this quantity. In the ratio many uncertainties get canceled and a precise determination of ξ would lead to a tight constraint on the CKM unitary triangle and hints for BSM physics in the form of an inconsistency of the unitary triangle in the SM.

Lattice QCD simulations including the b quark are, however, quite challenging, because of the large scale difference between light quarks (u and d) and the b quark. While fine lattice spacings are needed to correctly treat the b quark, a large volume is required to accommodate pion dynamics. Such a situation is difficult to achieve with current computational abilities. Heavy-quark effective theory (HQET) provides one realistic solution to this problem. In this formulation, the heavy (b) quark dynamics is integrated out and we may only treat the dynamics associated with light quarks. The theory is described by the systematic expansion of the inverse of the heavy-quark mass m_Q. A first attempt in this direction was carried out by Eichten and Hill [4,5], in which they used the static approximation (leading order of the heavy-quark mass expansion) and, for the static quark, they employed a standard static action. Soon after that attempt, however, it turned out that this approach leads to a poor signal-to-noise ratio (S/N) in correlation functions, because the static self-energy contains a notorious $1/a$ power divergence. (On the other hand, in nonrelativistic QCD—another effective theory approach—the power divergence tends to be canceled [6].) This situation has been significantly improved since the ALPHA Collaboration introduced the link-smearing technique in the static action, which partly cured the difficulty [7,8].

In this paper, we calculate B meson decay constants and neutral B meson mixing matrix elements using the static approximation. The static approximation always has $O(\Lambda_{\mathrm{QCD}}/m_b) \sim O(10\%)$ uncertainty, since the physical b-quark mass is not infinite. For SU(3)-breaking ratios like ξ or the ratio of B meson decay constants, however, the uncertainty coming from the static approximation is down to around the 2% level. This means that the static limit could be an especially good approximation compared with other lattice approaches that take into account the b-quark mass dependence for such ratios. To reduce the $O(\Lambda_{\mathrm{QCD}}/m_b)$ uncertainty in the HQET approach, higher-order operators in the $1/m_Q$ expansion need to be included. Taking into account these contributions requires nonperturbative matching with the continuum using, e.g., the Schrödinger functional scheme with a step-scaling technique [9], which requires considerable effort. Instead, we stay in the static limit assuming that the results can be valuable for an interpolation to the physical b-quark mass combined with lighter quark mass simulations, for which high-precision calculation is significantly important. (We discuss the meaning of calculations in the static limit in Sec. II.) This work is a first step toward the precise determination of B-physics quantities in the static limit.

This paper is organized as follows. In Sec. II, we discuss the meaning of the calculations in the static limit as an anchor point in the study of heavy-quark physics. In Sec. III, we summarize the physical observables in both full QCD theory and HQET, which we address for the study of neutral B meson mixing phenomena. In Sec. IV, the definition of lattice actions and the gluon ensembles that we use in this study are explained. In Sec. V, we describe the matching procedure between full QCD theory and HQET in the continuum, as well as between the continuum and lattice in HQET. The HQET matching is carried out by one-loop perturbation including $O(a)$ lattice errors. In Sec. VI, details of the measurement, correlator fits, and formulas for constructing physical quantities are shown. In Sec. VII, the chiral and continuum extrapolation formulas [SU(2)χPT] are summarized and we show the fit results. In Sec. VIII, we present the estimation of the systematic uncertainties and summarize it in Table XII. Finally, we present our final results, compare them with other works, and discuss future directions of this project in Sec. IX.

II. STATIC LIMIT AS A STRONG ANCHOR POINT

We employ the static approximation as a b-quark treatment in this study. As discussed earlier, this approximation suffers from an uncertainty of $O(10\%)$ for primary quantities or $O(2\%)$ for flavor SU(3)-breaking ratios at the physical b-quark mass, which is heavy but finite. The physical value of the approximation will eventually be lost as one aims for higher and higher precision. However, the results in the static limit are valuable as an anchor point when combined with simulations in the lower–quark-mass region. In this section we clarify the meaning of our calculations in the static limit.

We consider a heavy-quark expansion of some heavy-light quantity Φ_{hl}, which has a finite asymptotic limit as $m_Q \to \infty$,

$$\Phi_{\mathrm{hl}}(1/m_Q) = \Phi_{\mathrm{hl}}(0) \exp\left[\sum_{p=1}^{\infty} \gamma_p \left(\frac{\Lambda_{\mathrm{QCD}}}{m_Q}\right)^p\right], \qquad (4)$$

where m_Q is the heavy-quark mass, which is heavier than the QCD scale Λ_{QCD}. Equivalently, the expansion is written as

$$\Phi_{\mathrm{hl}}(1/m_Q) = \Phi_{\mathrm{hl}}(1/m_{Q_A}) \times \exp\left[\sum_{p=1}^{\infty} \gamma_p \left\{\left(\frac{\Lambda_{\mathrm{QCD}}}{m_Q}\right)^p - \left(\frac{\Lambda_{\mathrm{QCD}}}{m_{Q_A}}\right)^p\right\}\right], \qquad (5)$$

using some “anchor” point m_{Q_A}. [In Eq. (4) the static limit $m_Q \to \infty$ is regarded as an anchor point.] Our task is to determine the expansion coefficients γ_p and the overall factor $\Phi_{\mathrm{hl}}(1/m_{Q_A})$ to reach a physical b-quark point. There are several ways to make this determination.

(i) HQET approach: The anchor point is the static limit $m_Q \to \infty$. To treat the heavy-quark expansion from the static limit, HQET is employed. In addition to terms in the heavy-quark action and operators at the leading order of the expansion (static approximation), those at $O(1/m_Q)$ are included. To keep the theory renormalizable, the Boltzmann factor for the heavy quark is expanded in $1/m_Q$, and we make operator insertions in the expectation value evaluated with the static action. HQET must be matched with the original full theory. An important point is that the matching beyond the static approximation cannot be carried out perturbatively because of the existence of a $1/a$ power divergence in HQET [9,10].

(ii) Relativistic approach: The anchor point sits in a lower-mass region, typically the c-quark mass region. The usual relativistic formulations can be applicable in this region, while relatively finer lattices are required.

(iii) Combination of (i) and (ii) above: The anchor point is the static limit, while the γ_p's are explored by using usual relativistic formulations in a lower-quark mass region, i.e., the c-quark region (see, for example, Ref. [11]).

Procedure (i) has been used by the ALPHA Collaboration, in which nonperturbative matching with full QCD theory can be implemented by the step-scaling strategy with the Shcrödinger functional scheme [9]. (See Ref. [12] for their recent achievements.) In procedure (ii), relatively finer lattices with regular volume sizes are required. However, the lattices to treat the c quark are currently becoming available and approach (ii) is becoming feasible. A recent sophisticated implementation in this direction is the "ratio method" [13] of the ETM Collaboration, which may be a viable option. In this method, the ratios of physical quantities at some heavy-quark mass point m_Q and m_Q/λ with a scale parameter $\lambda > 1$, are considered to separate $\Phi_{\mathrm{hl}}(1/m_{Q_A})$ and the γ_p's in the determination:

$$\frac{\Phi_{\mathrm{hl}}(1/m_Q)}{\Phi_{\mathrm{hl}}(\lambda/m_Q)} = \exp\left[\sum_{p=1}^{\infty}\gamma_p(1-\lambda^p)\left(\frac{\Lambda_{\mathrm{QCD}}}{m_Q}\right)^p\right], \tag{6}$$

which enhances the precision of the γ_p's. (See Ref. [14] for their recent achievements.) A combination of the ratio method and the static limit as an anchor point would also be beneficial, which belongs to procedure (iii). In this sense, the static limit is not only of theoretical interest, but it is also a valuable anchor point to explore physics at the physical b-quark point. The fact that "the static limit is close to the physical b-quark mass in terms of $1/m_Q$" ensures the usefulness of the static limit as a "strong" anchor point.

III. PHYSICAL OBSERVABLES

A. Observables in full QCD theory

Our main aim in this paper is to calculate the CKM matrix elements V_{td} and V_{ts} to give constraints on the CKM unitary triangle. The current accuracy of the mass difference (1) from experiment is less than 1%, and thus a precise determination of the hadronic matrix element $\mathcal{M}_{B_q}$ would give strong constraints on the CKM matrix elements. We here summarize current world average values related with neutral B meson mixing, which are quoted from the Particle Data Group (PDG) [15]:

$$m_b(\overline{\mathrm{MS}}) = 4.18 \pm 0.03\ \mathrm{GeV}, \tag{7}$$

$$m_{B^0} = 5279.58 \pm 0.17\ \mathrm{MeV}, \tag{8}$$

$$m_{B_s^0} = 5366.77 \pm 0.24\ \mathrm{MeV}, \tag{9}$$

$$\begin{aligned}\Delta m_{B^0} &= (0.510 \pm 0.004) \times 10^{12}\hbar\mathrm{s}^{-1}\\ &= (3.337 \pm 0.033) \times 10^{-10}\ \mathrm{MeV},\end{aligned} \tag{10}$$

$$\begin{aligned}\Delta m_{B_s^0} &= (17.69 \pm 0.08) \times 10^{12}\hbar\mathrm{s}^{-1}\\ &= (1.164 \pm 0.005) \times 10^{-8}\ \mathrm{MeV}.\end{aligned} \tag{11}$$

Thus, the ratio of the CKM matrix elements (2) reads

$$\left|\frac{V_{td}}{V_{ts}}\right| = \xi \times (0.17071 \pm 0.00092), \tag{12}$$

which indicates that the determination of ξ with high accuracy would yield a precise value of the ratio.

The $\Delta B = 2$ mixing matrix element at a scale μ_b in the effective Hamiltonian is represented by

$$\begin{aligned}\mathcal{M}_{B_q}(\mu_b) &= \langle \bar{B}_q^0|[\bar{b}\gamma_\mu(1-\gamma_5)q][\bar{b}\gamma_\mu(1-\gamma_5)q]|B_q^0\rangle_{\mathrm{full}}\\ &\equiv \langle \bar{B}_q^0|O_L^{\mathrm{full}}|B_q^0\rangle_{\mathrm{full}},\end{aligned} \tag{13}$$

where b and q represent the b-quark and light (d or s) quark fields, respectively. In Eq. (13), we use a superscript and a subscript "full" to indicate that the theory considered here is not HQET, but rather full QCD theory. In this paper, the standard PDG notation for the quark content of the B meson is used: $B = (\bar{b}q)$ and $\bar{B} = (b\bar{q})$. The matrix element is conventionally parametrized as

$$\mathcal{M}_{B_q}(\mu_b) = \frac{8}{3}m_{B_q}^2 f_{B_q}^2 B_{B_q}(\mu_b), \tag{14}$$

so that $B_{B_q} = 1$ when the vacuum saturation approximation (VSA) exactly holds, where B_{B_q} denotes a dimensionless hadronic B parameter and f_{B_q} denotes the B_q meson decay constant defined by

$$if_{B_q}p_\mu = \langle 0|\bar{b}\gamma_\mu\gamma_5 q|B_q(p)\rangle_{\rm full} \equiv \langle 0|A_\mu^{\rm full}|B_q(p)\rangle_{\rm full}, \tag{15}$$

where p_μ is the four-momentum of the B_q meson. An RGI definition of the B parameters $\hat{B}_{B_q}$ is obtained from the B parameters in some scheme and at some scale μ_b by

$$\hat{B}_{B_q} = [\alpha_s(\mu_b)]^{-\frac{\gamma_0}{2\beta_0}}\left(1-\frac{\alpha_s(\mu_b)}{4\pi}Z_5\right)B_{B_q}(\mu_b), \tag{16}$$

at next-to-leading order (NLO), where Z_5—in the naive dimensional regularization (NDR) scheme with the modified minimal subtraction ($\overline{\rm MS}$) scheme—is written as [16]

$$Z_{n_f} = \frac{\gamma^{(1)}}{2\beta_0} - \frac{\gamma^{(0)}\beta_1}{2\beta_0^2}, \tag{17}$$

with

$$\beta_0 = 11 - \frac{2}{3}n_f, \qquad \beta_1 = 102 - \frac{38}{3}n_f, \tag{18}$$

$$\gamma^{(0)} = 4, \qquad \gamma^{(1)} = -7 + \frac{4}{9}n_f. \tag{19}$$

In this paper we use $\alpha_s(\mu_b) = 0.2265$, which is obtained from the strong coupling at the Z-boson mass scale $\alpha_s(m_Z = 91.1876(21)\ {\rm GeV}) = 0.1185(6)$ [15] using RG evolution (four loop [17,18]) with $n_f = 5$. Equation (16) thus becomes $\hat{B}_{B_q} = 1.516 \times B_{B_q}(\mu_b)$.

One of the main points of this paper is the SU(3)-breaking ratio (3), which should be unity in the SU(3) light flavor-symmetric case. In this ratio most of the theoretical uncertainties as well as the statistical fluctuations are largely canceled out. Using the parametrization of the matrix element (14), the SU(3)-breaking ratio is represented as

$$\xi = \frac{f_{B_s}}{f_B}\sqrt{\frac{B_{B_s}}{B_B}}. \tag{20}$$

Because the B parameters are based on the VSA by definition and there is a suppression factor due to SU(3) light flavor symmetry, the ratio of the B parameters in Eq. (20) could be close to one and a large fraction of the SU(3) breaking of ξ will likely reside in the ratio of the B meson decay constants.

B. Observables in the static limit

We regard the b quark as a heavy quark and give it an on-shell velocity $v_\mu = (1,0,0,0)$, which leads to an on-shell momentum $p_\mu = (m_b,0,0,0)$. The heavy-quark field h is introduced as a sum of a heavy quark h_+ and anti-heavy quark h_-:

$$h = h_+ + h_-, \quad \bar{h} = \bar{h}_+ + \bar{h}_- = h_+^\dagger - h_-^\dagger, \tag{21}$$

through

$$h_\pm = e^{\mp i m_b v\cdot x}\frac{1\pm \not{v}}{2}b = e^{\mp i m_b t}\frac{1\pm\gamma_0}{2}b, \tag{22}$$

where b is a usual relativistic quark field.

In the static limit, the B meson decay constant and the hadronic matrix element behave like $f_{B_q} \propto 1/\sqrt{m_{B_q}}$ and $\mathcal{M}_{B_q} \propto m_{B_q}$, respectively. Therefore it would be useful to introduce the quantities

$$\Phi_{B_q} = \sqrt{m_{B_q}}f_{B_q}, \qquad M_{B_q} = \frac{\mathcal{M}_{B_q}}{m_{B_q}}, \tag{23}$$

so that they behave as constants in the static limit. Hadron states in the HQET are labeled by v_μ and a residual momentum k_μ, which satisfies $v\cdot k = 0$. They are defined in the static limit and differ from those of the full QCD theory,

$$|B_q\rangle_{\rm full} = \sqrt{m_{B_q}}\{|B_q\rangle_{\rm HQET} + O(\Lambda_{\rm QCD}/m_b)\}, \tag{24}$$

so that the HQET state normalization becomes

$$\langle B_q(\vec{k})|B_q(\vec{k}')\rangle_{\rm HQET} = 2(2\pi)^3\delta^3(\vec{k}-\vec{k}'). \tag{25}$$

Using the HQET state, Φ_{B_q} in Eq. (23) is simply written as

$$\Phi_{B_q} = \langle 0|\bar{h}\gamma_0\gamma_5 q|B_q\rangle_{\rm HQET} \equiv \langle 0|A_0^{\rm HQET}|B_q\rangle_{\rm HQET}. \tag{26}$$

For M_{B_q}, we need two kinds of matrix elements,

$$M_L = \langle \bar{B}_q^0|[\bar{h}\gamma_\mu(1-\gamma_5)q][\bar{h}\gamma_\mu(1-\gamma_5)q]|B_q^0\rangle_{\rm HQET} \equiv \langle \bar{B}_q^0|O_L^{\rm HQET}|B_q^0\rangle_{\rm HQET}, \tag{27}$$

$$M_S = \langle \bar{B}_q^0|[\bar{h}(1-\gamma_5)q][\bar{h}(1-\gamma_5)q]|B_q^0\rangle_{\rm HQET} \equiv \langle \bar{B}_q^0|O_S^{\rm HQET}|B_q^0\rangle_{\rm HQET}, \tag{28}$$

owing to the lack of a four-dimensional Euclidean rotational symmetry in the static limit, where the $\Delta B = 2$ four-quark operator O_L is decomposed into spatial and time components,

$$\sum_{i=1,2,3}[\bar{h}\gamma_i(1-\gamma_5)q][\bar{h}\gamma_i(1-\gamma_5)q], \tag{29}$$

$$[\bar{h}\gamma_0(1-\gamma_5)q][\bar{h}\gamma_0(1-\gamma_5)q], \tag{30}$$

and they are renormalized differently. As a consequence, the operators (27) and (28) have mixings. In the following, the B meson states $|B_q\rangle$ and operators represent those in the static limit of the b quark unless stated otherwise.

IV. LATTICE ACTIONS AND GLUON ENSEMBLES

A. Lattice action

We perform lattice simulations in HQET, where the lattice action comprises three pieces:

$$S = S_{\mathrm{static}} + S_{\mathrm{DWF}} + S_{\mathrm{gluon}}, \tag{31}$$

where S_{static} is the static quark action representing the heavy (b) quark, S_{DWF} is the domain-wall fermion (DWF) action describing the light (u, d, s) quarks, and S_{gluon} is the gluon action.

1. Standard static heavy-quark action with link smearing

The standard static quark action [5] is given by

$$S_{\mathrm{static}} = \sum_x \bar{h}(x)\left\{\frac{1+\gamma_0}{2}[h(x) - U_0^\dagger(x-\hat{0})h(x-\hat{0})] - \frac{1-\gamma_0}{2}[U_0(x)h(x+\hat{0}) - h(x)]\right\}. \tag{32}$$

The lattice derivatives used here are not symmetric for each heavy and anti-heavy quark, and thus fermion doublers do not arise. The form of the action is technically the same as the Wilson quark action with a volume reduction to one dimension (time direction). Therefore it has a Wilson term, which decouples from any low-energy physics in the continuum limit and explicitly breaks the chiral symmetry at finite lattice spacing. This action suffers from huge $1/a$ power divergences, which results in tremendous noise in correlators. The solution to this problem is to introduce link smearing aimed at a reduction of the power divergences [8]. The modification is simply to replace the link variables $U_0(x)$ with three-step hypercubic blocked [19] ones $V_0(x)$, which are defined by

$$V_\mu(x) = \mathrm{Proj}_{\mathrm{SU(3)}}\left[(1-\alpha_1)U_\mu(x) + \frac{\alpha_1}{6}\sum_{\pm\nu\neq\mu}\tilde{V}_{\nu;\mu}(x)\tilde{V}_{\mu;\nu}(x+\hat{\nu})\tilde{V}^\dagger_{\nu;\mu}(x+\hat{\mu})\right], \tag{33}$$

$$\tilde{V}_{\mu;\nu}(x) = \mathrm{Proj}_{\mathrm{SU(3)}}\left[(1-\alpha_2)U_\mu(x) + \frac{\alpha_2}{4}\sum_{\pm\rho\neq\nu,\mu}\bar{V}_{\rho;\nu\mu}(x)\bar{V}_{\mu;\rho\nu}(x+\hat{\rho})\bar{V}^\dagger_{\rho;\nu\mu}(x+\hat{\mu})\right], \tag{34}$$

$$\bar{V}_{\mu;\nu\rho}(x) = \mathrm{Proj}_{\mathrm{SU(3)}}\left[(1-\alpha_3)U_\mu(x) + \frac{\alpha_3}{2}\sum_{\pm\eta\neq\rho,\nu,\mu}U_\eta(x)U_\mu(x+\hat{\eta})U^\dagger_\eta(x+\hat{\mu})\right], \tag{35}$$

where $\mathrm{Proj}_{\mathrm{SU(3)}}$ denotes an SU(3) projection and $(\alpha_1,\alpha_2,\alpha_3)$ are hypercubic blocking parameters [19]. $(\alpha_1,\alpha_2,\alpha_3) = (0,0,0)$ corresponds to an unsmeared link ($V_\mu = U_\mu$). We use two parameter choices in this work:

$$(\alpha_1,\alpha_2,\alpha_3) = \begin{cases} (0.75, 0.6, 0.3), & \text{HYP1 [19]}, \\ (1.0, 1.0, 0.5), & \text{HYP2 [18]}. \end{cases} \tag{36}$$

2. Domain-wall fermion action

The DWF action [20–22] is described by

$$S_{\mathrm{DWF}} = \sum_{s,s'=1}^{L_s}\sum_{x,y}\bar{\psi}_s(x)D^{\mathrm{DWF}}_{ss'}(x,y)\psi_{s'}(y) - \sum_x m_f\bar{q}(x)q(x), \tag{37}$$

$$D^{\mathrm{DWF}}_{ss'}(x,y) = D^4(x,y)\delta_{ss'} + D^5(s,s')\delta_{xy} + (M_5-5)\delta_{ss'}\delta_{xy}, \tag{38}$$

$$D^4(x,y) = \sum_\mu \frac{1}{2}[(1-\gamma_\mu)U_\mu(x)\delta_{x+\hat{\mu},y} + (1+\gamma_\mu)U^\dagger_\mu(y)\delta_{x-\hat{\mu},y}], \tag{39}$$

$$D^5(s,s') = \begin{cases} P_L\delta_{2,s'} & (s=1), \\ P_L\delta_{s+1,s'} + P_R\delta_{s-1,s'} & (1<s<L_s), \\ P_R\delta_{L_s-1,s'} & (s=L_s), \end{cases} \tag{40}$$

where $\psi_s(x)$ are $4+1$-dimensional fermion fields. The fifth dimension extends from 1 to L_s and is labeled by the indices s and s'. The domain-wall height (fifth-dimensional mass) M_5 is a parameter of the theory which can be set between $0 < M_5 < 2$. We use a setting of $M_5 = 1.8$. The physical four-dimensional quark field $q(x)$ is constructed from the fields $\psi_s(x)$ at $s = 1$ and L_s,

$$q(x) = P_L\psi_1(x) + P_R\psi_{L_s}(x), \tag{41}$$

$$\bar{q}(x) = \bar{\psi}_1(x)P_R + \bar{\psi}_{L_s}(x)P_L, \tag{42}$$

where P_L and P_R are left and right chirality projectors: $P_L = (1-\gamma_5)/2$, $P_R = (1+\gamma_5)/2$. In the infinite L_s limit, the right- and left-handed modes are decoupled and chiral symmetry is exactly restored. The presence of the chiral symmetry plays a crucial role in reducing unphysical operator mixing. Note that the DWF is automatically $O(a)$ improved [23].

3. Gluon action

We consider a class of RG-improved gluon actions in this study:

$$S_{\text{gluon}} = -\frac{2}{g_0^2}\left((1-8c_1)\sum_P \text{ReTr}[U_P] + c_1 \sum_R \text{ReTr}[U_R]\right), \tag{43}$$

where g_0 denotes the bare lattice coupling, U_P and U_R are the path-ordered product of links along a 1×1 plaquette P and the path-ordered product of links along a 1×2 rectangle R, respectively. Our choice of the parameter c_1 is -0.331 (Iwasaki gluon action) [24,25].

B. Gluon ensembles

We use $2+1$-flavor dynamical DWF gluon configurations generated by the RBC and UKQCD collaborations [26]. A summary of the ensembles used in this work is listed in Table I. Two lattice spacings, $a \sim 0.114$ fm and 0.0864 fm, are used to take a continuum limit. We label the coarser and finer lattices as "24c" and "32c," respectively, representing their lattice sizes. The physical box size is set to be modest, which is around 2.75 fm. The size of the fifth dimension $L_s = 16$, making the chiral symmetry breaking quite small with residual masses $m_{\text{res}} \simeq 0.003$ and 0.0007 for 24c and 32c, respectively. Degenerate u and d quark mass parameters are chosen so that the simulation covers the pion mass range 290–420 [MeV]. The smallest value of $m_\pi L$ is 4.06, which implies that the finite-volume (FV) effect would be small at simulation points. Only one sea s quark mass parameter is taken in our lattice ensemble for both lattice spacings, which is larger than the physical s quark mass by a small amount. As we will explain in Sec. VII, we basically use SU(2) chiral perturbation theory fit functions assuming that the sea s quark mass sits on a physical point, while the actual sea s quark mass in this simulation is not a physical one. The uncertainty from this inconsistency is estimated by the partially quenched SU(3) chiral perturbation theory as explained in Sec. VIII and turns out to be less than 1%. For a valence s quark, we make measurements with two s quark mass parameters that sandwich the physical s quark mass and make a linear interpolation.

V. MATCHING

In this work, we adopt a two-step matching: the first step is a matching between full QCD theory and HQET in the continuum, while the second is a matching between the continuum and the lattice in HQET. The matching is carried out by a one-loop perturbative calculation. Here we summarize the key points of the matching.

(i) The full theory operators in the continuum are renormalized in the $\overline{\text{MS}}$ (NDR) scheme at $\mu_b = m_b$, i.e., the b-quark mass scale. Fierz transformations in arbitrary dimensions are specified in the NDR scheme by Buras and Weisz evanescent operators [27].

(ii) The HQET operators in the continuum are also renormalized in the $\overline{\text{MS}}$ (NDR) scheme at some scale μ.

(iii) Matching operators between the full theory and HQET in the continuum are carried out by perturbatively calculating matrix elements of the operators in both theories and comparing them.

(iv) The matching above is performed at the scale $\mu = m_b$ to avoid a large logarithm of μ/m_b. We then use renormalization group running in the HQET to go down to a lower scale.

(v) The HQET operators with the lattice regularization are calculated using a DWF formalism for light quarks to maintain good chiral symmetry, which is important to control the operator mixing.

TABLE I. $2+1$-flavor dynamical domain-wall fermion ensembles by the RBC and UKQCD collaborations. [26] Physical quark masses are obtained using SU(2)χPT in the chiral extrapolation, and $m_{ud/s}^{\text{phys}} = m_{l/h}^{\text{phys}} + m_{\text{res}}(m_h^{\text{sim}})$.

Label	β	$L^3 \times T \times L_s$	a^{-1} [GeV]	a [fm]	aL [fm]	$m_{ud}^{\text{phys}}/m_s^{\text{phys}}$	$m_{\text{res}}(m_h^{\text{phys}})$	$m_{\text{res}}(m_h^{\text{sim}})$	m_l/m_h	$m_\pi(m_h^{\text{phys}})$ [MeV]	$m_\pi L$
24c1	2.13	$24^3 \times 64 \times 16$	1.729(25)	0.114	2.74	0.00134(4)/0.0379(11)	0.003076(58)	0.003152(43)	0.005/0.04	327	4.54
24c2									0.01/0.04	418	4.79
32c1	2.25	$32^3 \times 64 \times 16$	2.280(28)	0.0864	2.76	0.00100(3)/0.0280(7)	0.006643(82)	0.0006664(76)	0.004/0.03	289	4.06
32c2									0.006/0.03	344	4.83
32c3									0.008/0.03	393	5.52

(vi) Matching HQET operators between the continuum and the lattice is perturbatively carried out at a lattice cutoff scale $\mu = a^{-1}$, where a denotes a lattice spacing.

(vii) In the perturbative matching, we introduce a fictitious gluon mass to regulate IR divergences. The structure of the IR divergences should be the same between the continuum and the lattice theories, otherwise they cannot be matched to each other.

(viii) In the matching of HQET operators between the continuum and the lattice, $O(a)$ discretization errors are taken into account. We employ an on-shell $O(a)$ improvement program, in which we impose the equation of motion on the external heavy- and light-quark lines. In the improvement, we include both $O(pa)$ and $O(ma)$ contributions, where p and m denote the light-quark momentum and mass, respectively.

(ix) The theory with the static approximation of the heavy quark is renormalizable and perturbative renormalization is justified; however, this is impossible once the $O(1/m_Q)$ correction is included, in which case a nonperturbative subtraction of the $1/a$ power divergence is necessary [9,10]. The inclusion of the $O(a)$ improvement operators does not alter the justification of the perturbative treatment: the $O(a)$ operators just bring $O(\alpha_s^{k+1})$ uncertainty at the kth-loop perturbation by mixing with $O(a^0)$ operators, and do not cause destruction when taking a continuum limit.

In the following, the details are presented.

A. Continuum matching

In the continuum, the full QCD theory and HQET are renormalized at a scale μ, which we specify as a matching point. The operator relation of the heavy-light quark bilinear J_Γ and the $\Delta B = 2$ four-quark operator O_L between the two theories is written as

$$J_\Gamma^{\text{full}}(\mu) = C_\Gamma(\mu) J_\Gamma^{\text{HQET}}(\mu) + O(\Lambda_{\text{QCD}}/m_b), \qquad (44)$$

$$O_L^{\text{full}}(\mu) = Z_1(\mu) O_L^{\text{HQET}}(\mu) + Z_2(\mu) O_S^{\text{HQET}}(\mu) + O(\Lambda_{\text{QCD}}/m_b). \qquad (45)$$

The one-loop perturbative matching factor for the heavy-light axial-vector current is [4]

$$C_{\gamma_0\gamma_5}(\mu) = 1 + \left(\frac{g}{4\pi}\right)^2 \frac{4}{3}\left[-\frac{3}{2}\ln\left(\frac{\mu^2}{m_b^2}\right) - 2\right]. \qquad (46)$$

For the four-quark operator, the one-loop perturbative matching factors are [28,29]

TABLE II. Numerical values of the one-loop continuum matching factors and RG-running coefficients [30].

	24c (1.73 GeV)	32c (2.28 GeV)
$\alpha_s(m_b = 4.18$ GeV [15]$)$	0.2261	
$\alpha_s(m_c = 1.275$ GeV [15]$)$	0.3908	
$\alpha_s(a^{-1})$	0.3204	0.2773
$C_{\gamma_0\gamma_5}(m_b)$	0.9520	
$U_\Gamma^{N_f=4}(m_b, m_c)$	1.1550	
$U_\Gamma^{N_f=3}(m_c, a^{-1})$	0.9521	0.9196
$Z_1(m_b)$	0.7483	
$Z_2(m_b)$	−0.1439	
$U_L^{(11)N_f=4}(m_b, m_c)$	1.3345	
$U_L^{(21)N_f=4}(m_b, m_c)$	−0.0526	
$U_L^{(22)N_f=4}(m_b, m_c)$	1.0921	
$U_L^{(11)N_f=3}(m_c, a^{-1})$	0.9055	0.8442
$U_L^{(21)N_f=3}(m_c, a^{-1})$	0.0141	0.0231
$U_L^{(22)N_f=3}(m_c, a^{-1})$	0.9706	0.9500

$$Z_1(\mu) = 1 + \left(\frac{g}{4\pi}\right)^2\left[-6\ln\left(\frac{\mu^2}{m_b^2}\right) - 14\right], \qquad (47)$$

$$Z_2(\mu) = -8\left(\frac{g}{4\pi}\right)^2. \qquad (48)$$

The numerical values of the matching factors at $\mu = m_b$ are presented in Table II.

B. RG running in HQET

To avoid a large logarithm of μ/m_b, we match the theories at $\mu = m_b$ in the continuum matching and use RG running to reach a smaller energy scale μ in HQET. The running is governed by the RG equation:

$$\mu^2 \frac{d}{d\mu^2} C_\Gamma(\mu) = \frac{1}{2} C_\Gamma(\mu)\gamma_\Gamma, \qquad (49)$$

$$\mu^2 \frac{d}{d\mu^2}[Z_1(\mu) \quad Z_2(\mu)] = \frac{1}{2}[Z_1(\mu) \quad Z_2(\mu)]\begin{bmatrix} \gamma_{11} & \gamma_{12} \\ \gamma_{21} & \gamma_{22} \end{bmatrix}, \qquad (50)$$

where the γ's are anomalous dimensions. Solutions of the RG equations (49) and (50) are generally written as

$$C_\Gamma(\mu) = C_\Gamma(\mu') U_\Gamma(\mu', \mu), \qquad (51)$$

$$[Z_1(\mu) \quad Z_2(\mu)] = [Z_1(\mu') \quad Z_2(\mu')]\mathbf{U}_L(\mu', \mu), \qquad (52)$$

where

$$\mathbf{U}_L(\mu',\mu) = \begin{bmatrix} U_L^{(11)}(\mu',\mu) & U_L^{(12)}(\mu',\mu) \\ U_L^{(21)}(\mu',\mu) & U_L^{(22)}(\mu',\mu) \end{bmatrix}. \tag{53}$$

Note that heavy-quark spin symmetry gives constraints on the γ's:

$$\gamma_{12} = 0, \qquad \gamma_{22} = \gamma_{11} + 4\gamma_{21}, \tag{54}$$

which turn into

$$U_L^{(12)}(\mu',\mu) = 0, \tag{55}$$

$$U_L^{(22)}(\mu',\mu) = U_L^{(11)}(\mu',\mu) + 4U_L^{(21)}(\mu',\mu). \tag{56}$$

Each U is expressed as

$$U_\Gamma(\mu',\mu) = \left(1 + \frac{\alpha_s(\mu) - \alpha_s(\mu')}{4\pi} J_\Gamma\right) \left[\frac{\alpha_s(\mu')}{\alpha_s(\mu)}\right]^{d_\Gamma} + O(\alpha_s^2), \tag{57}$$

$$U_L^{(11)}(\mu',\mu) = \left(1 + \frac{\alpha_s(\mu) - \alpha_s(\mu')}{4\pi} J_1\right) \left[\frac{\alpha_s(\mu')}{\alpha_s(\mu)}\right]^{d_1} + O(\alpha_s^2), \tag{58}$$

$$U_L^{(21)}(\mu',\mu) = -\frac{1}{4}\left(\left[\frac{\alpha_s(\mu')}{\alpha_s(\mu)}\right]^{d_1} - \left[\frac{\alpha_s(\mu')}{\alpha_s(\mu)}\right]^{d_2}\right) + O(\alpha_s), \tag{59}$$

$$U_L^{(22)}(\mu',\mu) = \left[\frac{\alpha_s(\mu')}{\alpha_s(\mu)}\right]^{d_2} + O(\alpha_s), \tag{60}$$

where $\alpha_s = g^2/(4\pi)$. In the one-loop matching, two-loop calculations of the anomalous dimensions and a beta function are required to obtain J_Γ, d_Γ, J_1, d_1, and d_2 in Eqs. (57)–(60). The two-loop anomalous dimensions were calculated in Refs. [31,32] for quark bilinears and in Refs. [29,33,34] for four-quark operators.

Because we include sea quarks only for u, d, and s in our simulations ($N_f = 2+1$) and our lattice cutoff scale is higher than the c-quark mass, we employ a two-step RG running to reach a scale $\mu = a^{-1}$: we perform the running from $\mu = m_b$ to the m_c scale using $N_f = 4$ theory and running back to the a^{-1} scale using $N_f = 3$ theory, such as

$$U_\Gamma(m_b, a^{-1}) = U_\Gamma^{N_f=4}(m_b, m_c) U_\Gamma^{N_f=3}(m_c, a^{-1}), \tag{61}$$

$$\mathbf{U}_L(m_b, a^{-1}) = \mathbf{U}_L^{N_f=4}(m_b, m_c) \mathbf{U}_L^{N_f=3}(m_c, a^{-1}), \tag{62}$$

in which

$$d_\Gamma^{N_f=4} = -\frac{6}{25}, \quad d_1^{N_f=4} = -\frac{12}{25}, \quad d_2^{N_f=4} = -\frac{4}{25}, \tag{63}$$

$$J_\Gamma^{N_f=4} = 0.910, \qquad J_1^{N_f=4} = 1.864, \tag{64}$$

$$d_\Gamma^{N_f=3} = -\frac{2}{9}, \qquad d_1^{N_f=3} = -\frac{4}{9}, \qquad d_2^{N_f=3} = -\frac{4}{27}, \tag{65}$$

$$J_\Gamma^{N_f=3} = 0.755, \qquad J_1^{N_f=3} = 1.698. \tag{66}$$

The RG-running coefficients are summarized in Table II.

C. Static effective theory matching

The matching of the static effective theory between the continuum and the lattice is carried out at a scale $\mu = a^{-1}$ using one-loop perturbation. In the matching, lattice discretization errors are taken into account up to $O(pa)$ and $O(m_q a)$, where p and m_q are the typical light-quark momentum and light-quark mass, respectively. To include these discretization errors, higher-dimensional operators need to be added in the matching. The operator mixing pattern is constrained by symmetries, which are typically chiral symmetry, heavy-quark spin symmetry, and discrete symmetries, such as $\mathcal{P}$, $\mathcal{T}$, and $\mathcal{C}$.

The operator relation for the quark bilinear is written as

$$J_\Gamma^{\mathrm{cont}} = Z_\Gamma J_\Gamma^{\mathrm{imp}}, \tag{67}$$

where J_Γ^{imp} is the $O(a)$-improved lattice bilinear,

$$J_\Gamma^{\mathrm{imp}} = J_\Gamma + a c_\Gamma^{(pa)} G J_{\Gamma D} + a c_\Gamma^{(ma)} G J_{\Gamma M}, \tag{68}$$

in which

$$J_{\Gamma D} = \bar{h}\Gamma(\gamma \cdot \vec{\boldsymbol{D}})q, \qquad J_{\Gamma M} = m_q \bar{h}\Gamma q, \tag{69}$$

and G is defined by $\gamma_0 \Gamma \gamma_0 = G\Gamma$. For the four-quark operators,

$$O_L^{\mathrm{cont}} = Z_L O_L^{\mathrm{imp}}, \tag{70}$$

$$O_S^{\mathrm{cont}} = Z_S O_S^{\mathrm{imp}}, \tag{71}$$

where O_L^{imp} and O_S^{imp} are $O(a)$-improved lattice operators,

$$\begin{aligned} O_L^{\mathrm{imp}} = O_L &+ a c_L^{(pa)}(O_{ND} + 2O'_{ND}) \\ &+ a c_L^{(ma)}(O_{NM} + 2O'_{NM}), \end{aligned} \tag{72}$$

$$\begin{aligned} O_S^{\mathrm{imp}} = O_S &+ a c_S^{(pa)}(O_{ND} - 2O'_{ND}) \\ &+ a c_S^{(ma)}(O_{NM} - 2O'_{NM}), \end{aligned} \tag{73}$$

with

$$O_{ND} = 2[\bar{h}\gamma_\mu^R(\boldsymbol{\gamma}\cdot\vec{\boldsymbol{D}})q][\bar{h}\gamma_\mu^L q], \tag{74}$$

$$O'_{ND} = 2[\bar{h}P_R(\boldsymbol{\gamma}\cdot\vec{\boldsymbol{D}})q][\bar{h}P_L q], \tag{75}$$

$$O_{NM} = 2m_q[\bar{h}\gamma_\mu^R q][\bar{h}\gamma_\mu^L q], \tag{76}$$

$$O'_{NM} = 2m_q[\bar{h}P_R q][\bar{h}P_L q]. \tag{77}$$

We note that the coefficients for the quark bilinear operator do not depend on Γ, which is a consequence of chiral and heavy-quark spin symmetry [30,35,36], and this fact holds nonperturbatively. [For the four-quark operators, it is claimed that more higher-order operators are required in Eqs. (72) and (73) for the $O(a)$ improvement at higher-loop or nonperturbative levels [37].]

For the one-loop calculation of the coefficients in Eqs. (67), (70), and (71), we use mean-field (MF) improvement to remove huge the tadpole contribution in the lattice perturbation [38]. The measured plaquette value P or $u_0 = P^{1/4}$ enters the matching for the MF improvement.

We employ DWF as light quarks, and thus the physical light-quark propagator is written as

$$\begin{aligned} S_q(p) &= \langle q(-p)\bar{q}(p)\rangle \\ &= \frac{1-w_0^2}{i\not{p} + (1-w_0^2)m_f}(1 + O(p^2, pm_f, m_f^2)), \end{aligned} \tag{78}$$

where $w_0 = 1 - M_5$. The physical quark propagator suggests that the quark wave function has a domain-wall-specific factor $(1-w_0^2)^{1/2}$ and the quark mass should be identified by $m_q = (1-w_0^2)m_f$, which would appear in the matching coefficients.

The matching coefficients at the one-loop level are

$$Z_\Gamma = \mathcal{Z}_w^{-1/2}\left\{1 + \left(\frac{g_{\overline{\rm MS}}}{4\pi}\right)^2 \frac{4}{3}\hat{z}_\Gamma^{\rm MF}\right\} + O(g^4), \tag{79}$$

$$c_\Gamma^{(pa)} = \frac{1}{u_0}\left(\frac{g_{\overline{\rm MS}}}{4\pi}\right)^2 \frac{4}{3}\hat{z}_\Gamma^{\rm (pa)MF} + O(g^4), \tag{80}$$

$$c_\Gamma^{(ma)} = \frac{1}{u_0}\left(\frac{g_{\overline{\rm MS}}}{4\pi}\right)^2 \frac{4}{3}\hat{z}_\Gamma^{\rm (ma)MF} + O(g^4), \tag{81}$$

$$Z_L = \mathcal{Z}_w^{-1}\left\{1 + \left(\frac{g_{\overline{\rm MS}}}{4\pi}\right)^2 \frac{4}{3}\hat{z}_L^{\rm MF}\right\} + O(g^4), \tag{82}$$

$$c_L^{(pa)} = \frac{1}{u_0}\left(\frac{g_{\overline{\rm MS}}}{4\pi}\right)^2 \frac{4}{3}\hat{z}_L^{\rm (pa)MF} + O(g^4), \tag{83}$$

$$c_L^{(ma)} = \frac{1}{u_0}\left(\frac{g_{\overline{\rm MS}}}{4\pi}\right)^2 \frac{4}{3}\hat{z}_L^{\rm (ma)MF} + O(g^4), \tag{84}$$

$$Z_S = \mathcal{Z}_w^{-1} + O(g^2), \tag{85}$$

TABLE III. Numerical values of the one-loop static effective theory matching factors [30].

	24c		32c	
	HYP1	HYP2	HYP1	HYP2
P (chiral limit)	0.5883		0.6156	
$M_5^{\rm MF}$	1.3032		1.3432	
$g_{\overline{\rm MS}}^2/4\pi$	0.1769		0.1683	
$Z_{\Gamma=\gamma_0\gamma_5}$	0.9105	0.9383	0.9256	0.9526
$c_{\Gamma=\gamma_0\gamma_5}^{(pa)}$	0.0790	0.1374	0.0744	0.1294
$c_{\Gamma=\gamma_0\gamma_5}^{(ma)}$	0.0864	0.1660	0.0739	0.1482
Z_L	0.8260	0.8911	0.8546	0.9187
$c_L^{(pa)}$	0.1185	0.2061	0.1117	0.1942
$c_L^{(ma)}$	0.1296	0.2489	0.1108	0.2222
Z_S	0.9645		1.0040	

$$c_S^{(pa)} = O(g^2), \tag{86}$$

$$c_S^{(ma)} = O(g^2), \tag{87}$$

where

$$\mathcal{Z}_w = \frac{1-(w_0^{\rm MF})^2}{u_0}\left(1 + \left(\frac{g_{\overline{\rm MS}}}{4\pi}\right)^2 \frac{4}{3}\hat{z}_w^{\rm MF}\right) + O(g^4), \tag{88}$$

and the renormalized coupling in the continuum $\overline{\rm MS}$ scheme $g_{\overline{\rm MS}}$ at the scale $\mu = a^{-1}$ is related to the bare lattice coupling g_0 as

$$\frac{1}{g_{\overline{\rm MS}}^2} = \frac{P}{g_0^2} + d_g + c_p + N_f d_f, \tag{89}$$

in which d_g and c_p are dependent on the gluon action and d_f is dependent on the fermion action. Note that the continuum matching coefficient for O_S is already $O(g^2)$; therefore, only the tree-level static matching coefficient for this operator is needed in the one-loop matching procedure. Nevertheless, we partly include the $O(g^2)$ in Eq. (85) to keep the same form of $\mathcal{Z}_w$ as that for Z_L, which does not matter at the one-loop level. The coefficients for this simulation are summarized in Table III.

VI. MEASUREMENT AND DATA EXTRACTION

In this section, we present details of measurements on the gluon configurations introduced in Sec. IV.

A. Correlators

In the static limit, the energies of states do not depend on their momentum. This fact requires special treatment of the correlators, because even with a large separation of the source and sink positions in time t, a unique ground state cannot be obtained [39,40]. In particular, the Gaussian source and sink smearing used in this work requires taking this feature into account. In this subsection, we follow the discussions in Refs. [39,40] and explicitly show an extension to any form of source- and sink-smearing function.

We start with defining our state convention. The static action (32) is invariant under a spatial local phase rotation of heavy-quark fields,

$$h(\vec{x},t) \longrightarrow e^{i\theta(\vec{x})} h(\vec{x},t), \tag{90}$$

$$\bar{h}(\vec{x},t) \longrightarrow e^{-i\theta(\vec{x})} \bar{h}(\vec{x},t), \tag{91}$$

which leads to Noether's current,

$$J_h(\vec{x},t) = \bar{h}(\vec{x},t) h(\vec{x},t), \tag{92}$$

with the conservation law

$$\partial_0 J_h(\vec{x},t) = 0 \tag{93}$$

indicating the time-independent charge (heavy-quark number density operator) at each spatial point,

$$N_h(\vec{x}) = J_h(\vec{x},t), \tag{94}$$

which commutes with the Hamiltonian. We can define B meson states in the PDG notation, $B = (\bar{b}q)$ and $\bar{B} = (b\bar{q})$, as eigenstates of $N_h(\vec{x})$,

$$N_h(\vec{y})|\tilde{B}(\vec{x})\rangle_L = -\delta^{(3)}_{\vec{x},\vec{y}} |\tilde{B}(\vec{x})\rangle_L, \tag{95}$$

$$\langle \tilde{B}(\vec{x})|\tilde{B}(\vec{y})\rangle_L = \delta^{(3)}_{\vec{x},\vec{y}}, \tag{96}$$

where "L" indicates states in the static limit with finite spatial size L. Using these, the B meson states with spacial momentum $\vec{p}$ are defined as

$$|B(\vec{p})\rangle_L = \sqrt{2a^3} \sum_{\vec{x}} e^{-i\vec{p}\cdot\vec{x}} |\tilde{B}(\vec{x})\rangle_L, \tag{97}$$

where the momentum $\vec{p}$ takes discrete values:

$$\vec{p} = \frac{2\pi}{La}(n_1, n_2, n_3), \qquad 0 < n_1, n_2, n_3 \leq L. \tag{98}$$

This state convention gives the normalization

$$\langle B(\vec{p})|B(\vec{q})\rangle_L = 2(La)^3 \delta^{(3)}_{\vec{p},\vec{q}} \underset{La\to\infty}{\longrightarrow} 2(2\pi)^3 \delta^{(3)}(\vec{p}-\vec{q}), \tag{99}$$

which leads to a relation between the finite- and infinite-volume momentum eigenstates,

$$|B(\vec{p})\rangle_L \underset{La\to\infty}{\longrightarrow} |B(\vec{p})\rangle, \tag{100}$$

$$\langle B(\vec{p})|B(\vec{q})\rangle = 2(2\pi)^3 \delta^{(3)}(\vec{p}-\vec{q}), \tag{101}$$

so that infinite-volume static states $|B(\vec{p})\rangle$ give the conventional normalization (101). Thus, what we need to calculate in the finite volume are

$$\langle 0|A_0(\vec{0},0)|B(\vec{p}=0)\rangle_L \underset{La\to\infty}{\longrightarrow} \Phi_B, \tag{102}$$

$$\langle B(\vec{p}=0)|O_{4\mathrm{q}}(\vec{0},0)|B(\vec{p}=0)\rangle_L \underset{La\to\infty}{\longrightarrow} M_B, \tag{103}$$

where $A_0(\vec{x},t)$ and $O_{4\mathrm{q}}(\vec{x},t)$ are the local heavy-light axial-vector current (in the time direction) and four-quark operators defined in Eqs. (26), (27), and (28). The statement made earlier in this subsection that the B meson energy does not depend on its momentum is understandable, as the B meson states defined in Eq. (95) are also energy eigenstates, where the energy does not depend on spatial coordinates due to the translational invariance of the system, and as a consequence the energy is independent of the momentum by Eq. (97). This property requires an unfamiliar treatment of the correlators. A typical example is an operator which includes a spatially smeared quark field:

$$A_0^S(\vec{x},t) = \left(\sum_{\vec{y}} f(\vec{y}) \bar{h}(\vec{x}+\vec{y},t)\right)\gamma_0\gamma_5 \cdot \left(\sum_{\vec{z}} g(\vec{z}) q(\vec{x}+\vec{z},t)\right), \tag{104}$$

where $f(\vec{y})$ and $g(\vec{z})$ are smearing functions, such as Gaussian- and wall-type functions. We consider the B meson decay amplitude with the smeared operator and take the large-t limit:

$$\begin{aligned} &\langle 0|A_0^S(\vec{x},t)|B(\vec{p})\rangle_L \\ &\underset{t\gg 0}{\longrightarrow} e^{i\vec{p}\cdot\vec{x}} e^{-E_0 t} \langle 0|A_0^S(\vec{0},0)|B(\vec{p})\rangle_L \\ &\neq \delta^{(3)}_{\vec{p},\vec{0}} e^{-E_0 t} \langle 0|A_0^S(\vec{0},0)|B(\vec{p}=0)\rangle_L, \end{aligned} \tag{105}$$

where E_0 represents the energy of the B meson ground state. Thus we cannot obtain a unique zero-momentum state even in the large-t limit, because the B meson energy no longer depends on the spatial momentum $\vec{p}$. This fact causes an unusual derivation of the matrix elements. Let us demonstrate this here. We consider a three-point (3PT) function with smeared quark fields,

$$C^{SS}_{4\mathrm{q}}(t_f,t,0) = a^3 \sum_{\vec{x}} \langle A_0^S(\vec{0},t_f) O_{4\mathrm{q}}(\vec{x},t) A_0^{S\dagger}(\vec{0},0)\rangle. \tag{106}$$

Using the completeness of the states,

$$\mathbf{1} = \frac{1}{2(La)^3}\sum_{\vec{p}}|B(\vec{p})\rangle_L\langle B(\vec{p})| + (\text{higher states}), \tag{107}$$

the 3PT function becomes

$$\begin{aligned}
&\mathcal{C}^{SS}_{4\mathrm{q}}(t_f,t,0)\\
&\xrightarrow[t_f\gg t\gg 0]{} \frac{1}{4(La)^3}\sum_{\vec{p}} e^{-E_0 t_f}\langle 0|A_0^S(\vec{0},0)|B(\vec{p})\rangle_L\\
&\qquad\cdot\langle B(\vec{p})|O_{4\mathrm{q}}(\vec{0},0)|B(\vec{p})\rangle_L\langle B(\vec{p})|A_0^{S\dagger}(\vec{0},0)|0\rangle_L\\
&\qquad= \frac{1}{2}\mathcal{C}^{SS}(t_f,0)M_B,
\end{aligned} \tag{108}$$

where

$$\begin{aligned}
\mathcal{C}^{SS}(t,0) &= \langle A_0^S(\vec{0},t)A_0^{S\dagger}(\vec{0},0)\rangle\\
&\xrightarrow[t\gg 0]{} \frac{1}{2(La)^3}e^{-E_0 t}\sum_{\vec{p}}|\langle 0|A_0^S(\vec{0},0)|B(\vec{p})\rangle_L|^2\\
&= \mathcal{A}^{SS}e^{-E_0 t},
\end{aligned} \tag{109}$$

and we used

$$\begin{aligned}
&\langle B(\vec{p})|O_{4\mathrm{q}}(\vec{0},0)|B(\vec{p})\rangle_L\\
&\quad= \langle B(\vec{p}=0)|O_{4\mathrm{q}}(\vec{0},0)|B(\vec{p}=0)\rangle_L,
\end{aligned} \tag{110}$$

following Eq. (97). As can be seen in Eq. (108), we inevitably have to use $\mathcal{C}^{SS}(t,0)$, in which the sink position is not spatially volume summed, which results in large statistical noise. The matrix element M_B is then obtained as

$$\mathcal{C}^{SS}_{4\mathrm{q}}(t_f,t,0)\xrightarrow[t_f\gg t\gg 0]{}\mathcal{A}_{4\mathrm{q}}, \tag{111}$$

$$M_B = \frac{2\mathcal{A}_{4\mathrm{q}}}{\mathcal{A}^{SS}e^{-E_0 t_f}}. \tag{112}$$

To obtain a zero-momentum state in the two-point (2PT) functions, we have to use a projection by spatial volume summation of the sink operator. What we need to measure for Φ_B are the 2PT correlation functions,

$$\mathcal{C}^{\tilde{L}S}(t,0) = a^3\sum_{\vec{x}}\langle A_0(\vec{x},t)A_0^{S\dagger}(\vec{0},0)\rangle, \tag{113}$$

$$\mathcal{C}^{\tilde{S}S}(t,0) = a^3\sum_{\vec{x}}\langle A_0^S(\vec{x},t)A_0^{S\dagger}(\vec{0},0)\rangle, \tag{114}$$

in which the sink operators are volume summed to project into the zero-momentum state; otherwise, we cannot obtain a unique state by just taking the large-t limit. By using the completeness of states [Eq. (107)], these 2PT correlation functions in $t \gg 0$ can be easily written as

$$\begin{aligned}
\mathcal{C}^{\tilde{L}S}(t,0)&\xrightarrow[t\gg 0]{}\frac{1}{2}\langle 0|A_0(\vec{0},0)|B(\vec{p}=0)\rangle_L\\
&\qquad\times\langle B(\vec{p}=0)|A_0^S(\vec{0},0)|0\rangle_L e^{-E_0 t}\\
&\qquad= \mathcal{A}^{\tilde{L}S}e^{-E_0 t},
\end{aligned} \tag{115}$$

$$\begin{aligned}
\mathcal{C}^{\tilde{S}S}(t,0)&\xrightarrow[t\gg 0]{}\frac{1}{2}|\langle 0|A_0^S(\vec{0},0)|B(\vec{p}=0)\rangle_L|^2 e^{-E_0 t}\\
&\qquad= \mathcal{A}^{\tilde{S}S}e^{-E_0 t}.
\end{aligned} \tag{116}$$

Φ_B is then obtained through

$$\Phi_B \xrightarrow[t\gg 0]{} \sqrt{2}\frac{\mathcal{C}^{\tilde{L}S}(t,0)}{\sqrt{\mathcal{C}^{\tilde{S}S}(t,0)e^{-E_0 t}}} = \sqrt{2}\frac{\mathcal{A}^{\tilde{L}S}}{\sqrt{\mathcal{A}^{\tilde{S}S}}}, \tag{117}$$

in which the noisy correlator $\mathcal{C}^{SS}(t,0)$ is not needed, in contrast to M_B. In the actual simulation, we use $O(a)$-improved operators to remove the $O(a)$ lattice artifact, as indicated in Eqs. (68), (72), and (73) in Sec. V.

B. Source and sink smearing

In an attempt to obtain a better overlap with the ground state, we use gauge-invariant Gaussian smearing for the source and sink operators. We follow the smearing procedure in Refs. [41,42]. We choose a Gaussian function with width ω as a smearing function in Eq. (104) for both static and light quarks:

$$f(\vec{x}) = g(\vec{x}) = \exp(-x^2/\omega^2). \tag{118}$$

To achieve this smearing in a gauge-invariant way, we use the implementation

$$\sum_{\vec{y}} f(\vec{y})\psi(\vec{x}+\vec{y},t) = \left(1+\frac{\omega^2}{4N_G}\nabla^2\right)^{N_G}\psi(\vec{x},t), \tag{119}$$

with the hopping matrix

$$[\nabla^2]_{xy} \equiv \sum_{i=1}^{3}[U_i(x+\hat{i})\delta_{x+\hat{i},y} + U_i^\dagger(x-\hat{i})\delta_{x-\hat{i},y}], \tag{120}$$

where N_G is the number of times the smearing kernel acts on the fermion field $\psi(\vec{x},t)$, which leads to the Gaussian function (118) in the $N_G \to \infty$ limit. The choices for the parameters ω and N_G are summarized in Table IV, which gives a physical Gaussian width around 0.45 fm.

C. Measurement parameters

The measurement parameters are summarized in Table IV. The valence d quark mass parameter is the same as the degenerate sea u and d quarks. To interpolate to a physical s quark mass, we take two values of the s valence

TABLE IV. Measurement parameters. N_G and ω are the source and sink Gaussian smearing parameters. $\Delta t_{\text{src-sink}}$ represents the source-sink separation in the three-point functions.

Label	m_q	Measured MD traj.	# of data	# of src	N_G	ω	$\Delta t_{\text{src-sink}}$
24c1	0.005, 0.034, 0.040	900–8980 every 40	203	4	32	4	20
24c2	0.010, 0.034, 0.040	1460–8540 every 40	178	2			
32c1	0.004, 0.027, 0.030	520–6800 every 20	304	1	40	5	24
32c2	0.006, 0.027, 0.030	1000–7220 every 20	312	1			
32c2	0.008, 0.027, 0.030	520–5540 every 20	252	1			

quark mass parameters that sandwich the physical point, and one of them is set to be the same as the sea s quark's value. The physical s quark mass is slightly different from the sea s quark mass, so we estimate the uncertainty from this inconsistency by using the partially quenched SU(3) chiral perturbation theory, which we describe later.

D. Autocorrelations

The autocorrelation time of the ensemble is investigated using the integrated autocorrelation time for both static heavy-light two-point and three-point functions. The integrated autocorrelation time of the 2PT functions is measured at $t = 12$ for $\mathcal{C}^{\tilde{L}S}(t,0)$ and $\mathcal{C}^{\tilde{S}S}(t,0)$, but at $t = 15$ for $\mathcal{C}^{SS}(t,0)$ in both the 24c and 32c ensembles. We measure it at the midpoint between the source and sink locations for the 3PT functions. Based on this analysis, we choose to perform blocking, so that the blocking size is 80 MD trajectories for the 32c1 ensemble (the lightest quark mass parameter), whereas it is 40 MD trajectories for other ensembles. Note that in the study of the light hadron spectrum on these ensembles, the blocking size was 20 MD trajectories [26].

E. Correlator fits

In the figures in Appendix A, we show the effective masses of the 2PT functions and the amplitudes of the 3PT functions. We perform simultaneous fits of three types of 2PT correlators [$\mathcal{C}^{\tilde{L}S}(t,0)$, $\mathcal{C}^{\tilde{S}S}(t,0)$, and $\mathcal{C}^{SS}(t,0)$] assuming that E_0 is common in these correlators. To take the periodicity in the lattice box into account, a cosh function is assumed in the fit:

$$\mathcal{C}^{\tilde{L}S}(t,0) = \mathcal{A}^{\tilde{L}S}(e^{-E_0 t} + e^{-E_0(T-t)}), \tag{121}$$

$$\mathcal{C}^{\tilde{S}S}(t,0) = \mathcal{A}^{\tilde{S}S}(e^{-E_0 t} + e^{-E_0(T-t)}), \tag{122}$$

$$\mathcal{C}^{SS}(t,0) = \mathcal{A}^{SS}(e^{-E_0 t} + e^{-E_0(T-t)}). \tag{123}$$

For the 3PT correlators $\mathcal{C}_L^{SS}(t_f,t,0)$ and $\mathcal{C}_S^{SS}(t_f,t,0)$, constant fits are made:

$$\mathcal{C}_L^{SS}(t_f,t,0) = \mathcal{A}_L^{SS}, \tag{124}$$

$$\mathcal{C}_S^{SS}(t_f,t,0) = \mathcal{A}_S^{SS}, \tag{125}$$

where t_f is fixed to be the source-sink separation shown in Table IV. Fit ranges are shown in the effective mass and amplitude plots in Appendix A, and the fit results are presented in Tables V and VI. Note that the $O(a)$-improved $\mathcal{C}_S^{SS}(t_f,t,0)$ is not calculated, as the one-loop level matching does not require it.

For some quark mass parameters, $\chi^2/\text{d.o.f.}$ exceeds 2. We, however, keep fit ranges unaltered throughout all quark mass parameters, to avoid human bias. Then our correlator fit results have a non-negligible fit-range dependence. As we will explain in Sec. VIII I, the fit-range dependencies are taken into account as an uncertainty of our calculation.

F. Decay constants, matrix elements, and *B* parameters

The B meson decay constants f_B and mixing matrix elements $\mathcal{M}_B$ are obtained by Eq. (23) through Eqs. (117) and (112). The results obtained are presented in Table VII. The statistical error at each simulation point is less than 2% for decay constants, while it sometimes reaches 5% for matrix elements and B parameters.

VII. CHIRAL/CONTINUUM EXTRAPOLATION

A. NLO SU(2)HMχPT formula

Physical quantities at simulated light (u and d) quark mass points are extrapolated to the physical degenerate light-quark value. In this work, we use next-to-leading-order SU(2) heavy-light meson chiral perturbation theory [NLO SU(2)HMχPT], depicted in Ref. [40]. [See also Ref. [43] for SU(2)χPT.] In SU(2)χPT, the s quark is integrated out of the theory; effects from the s quark are included in low-energy constants (LECs). The SU(2)χPT formula is obtained from SU(3)χPT assuming that the u- and d-quark masses are much smaller than the s-quark mass. The formula does not depend on the s-quark mass in an explicit way. The convergence of the chiral fit is improved by using the SU(2)χPT as long as the u- and d-quark masses are sufficiently small [43]. In Ref. [43], it was argued that the RBC/UKQCD DWF ensemble does not show convergence of NLO SU(2)χPT above a pion mass of 420 MeV for the light hadron masses and decay constants. The ensembles we use in this work stay below this border.

TABLE V. Correlator fit results [$O(a)$ unimproved].

24c1, $m_h = 0.040$, $m_l = 0.005$

Smear	m_q	E_0	$\mathcal{A}^{\tilde{L}S}$	$\mathcal{A}^{\tilde{S}S}$	$\mathcal{A}^{SS}$	χ^2/d.o.f.	$\mathcal{A}^{SS}_L$	χ^2/d.o.f.	$\mathcal{A}^{SS}_S$	χ^2/d.o.f.
HYP1	0.005	0.5107(28)	0.1291(33)e + 5	0.1386(33)e + 10	0.2663(66)e + 7	1.3	0.294(13)e + 2	0.5	−0.1741(61)e + 2	0.5
	0.034	0.5440(13)	0.1542(18)e + 5	0.1512(16)e + 10	0.2984(40)e + 7	1.5	0.2230(43)e + 2	0.6	−0.1357(24)e + 2	0.5
	0.04	0.5510(12)	0.1589(17)e + 5	0.1531(15)e + 10	0.3038(38)e + 7	1.4	0.2064(37)e + 2	0.6	−0.1262(21)e + 2	0.4
HYP2	0.005	0.4656(22)	0.1124(23)e + 5	0.1407(28)e + 10	0.2670(56)e + 7	1.2	0.509(15)e + 2	0.4	−0.3258(89)e + 2	0.2
	0.034	0.4998(11)	0.1330(13)e + 5	0.1543(14)e + 10	0.3041(33)e + 7	2.1	0.3789(64)e + 2	0.4	−0.2412(40)e + 2	0.6
	0.04	0.5073(10)	0.1370(12)e + 5	0.1565(13)e + 10	0.3099(32)e + 7	2.1	0.3487(55)e + 2	0.5	−0.2221(35)e + 2	0.7

24c2, $m_h = 0.040$, $m_l = 0.01$

Smear	m_q	E_0	$\mathcal{A}^{\tilde{L}S}$	$\mathcal{A}^{\tilde{S}S}$	$\mathcal{A}^{SS}$	χ^2/d.o.f.	$\mathcal{A}^{SS}_L$	χ^2/d.o.f.	$\mathcal{A}^{SS}_S$	χ^2/d.o.f.
HYP1	0.01	0.5117(36)	0.1291(42)e + 5	0.1368(42)e + 10	0.276(10)e + 7	1.8	0.299(16)e + 2	1.0	−0.1850(81)e + 2	1.0
	0.034	0.5408(22)	0.1493(30)e + 5	0.1475(27)e + 10	0.3043(69)e + 7	1.8	0.2288(73)e + 2	1.1	−0.1424(39)e + 2	0.5
	0.04	0.5480(20)	0.1540(28)e + 5	0.1494(25)e + 10	0.3095(65)e + 7	1.8	0.2115(63)e + 2	1.2	−0.1322(34)e + 2	0.6
HYP2	0.01	0.4645(30)	0.1094(30)e + 5	0.1351(36)e + 10	0.2706(83)e + 7	0.9	0.547(20)e + 2	1.2	−0.344(11)e + 2	0.7
	0.034	0.4955(17)	0.1269(21)e + 5	0.1477(23)e + 10	0.3002(54)e + 7	1.1	0.3986(94)e + 2	1.0	−0.2543(62)e + 2	0.7
	0.04	0.5033(16)	0.1309(20)e + 5	0.1501(22)e + 10	0.3062(52)e + 7	1.2	0.3648(82)e + 2	1.0	−0.2333(54)e + 2	0.7

32c1, $m_h = 0.030$, $m_l = 0.004$

Smear	m_q	E_0	$\mathcal{A}^{\tilde{L}S}$	$\mathcal{A}^{\tilde{S}S}$	$\mathcal{A}^{SS}$	χ^2/d.o.f.	$\mathcal{A}^{SS}_L$	χ^2/d.o.f.	$\mathcal{A}^{SS}_S$	χ^2/d.o.f.
HYP1	0.004	0.4231(29)	0.753(19)e + 4	0.1195(30)e + 10	0.1105(32)e + 7	0.4	0.481(44)e + 1	0.5	−0.284(21)e + 1	0.5
	0.027	0.4519(14)	0.925(12)e + 4	0.1343(16)e + 10	0.1262(21)e + 7	0.6	0.379(15)e + 1	0.7	−0.2264(83)e + 1	1.0
	0.03	0.4557(14)	0.945(12)e + 4	0.1355(15)e + 10	0.1278(20)e + 7	0.7	0.363(14)e + 1	0.7	−0.2170(77)e + 1	1.1
HYP2	0.004	0.3816(28)	0.674(16)e + 4	0.1198(28)e + 10	0.1096(28)e + 7	1.0	0.1041(73)e + 2	2.0	−0.661(33)e + 1	0.1
	0.027	0.4118(14)	0.832(10)e + 4	0.1365(16)e + 10	0.1280(19)e + 7	1.4	0.802(23)e + 1	2.2	−0.496(15)e + 1	0.8
	0.03	0.4157(14)	0.849(10)e + 4	0.1379(15)e + 10	0.1296(19)e + 7	1.5	0.764(21)e + 1	2.2	−0.473(13)e + 1	0.9

32c2, $m_h = 0.030$, $m_l = 0.006$

Smear	m_q	E_0	$\mathcal{A}^{\tilde{L}S}$	$\mathcal{A}^{\tilde{S}S}$	$\mathcal{A}^{SS}$	χ^2/d.o.f.	$\mathcal{A}^{SS}_L$	χ^2/d.o.f.	$\mathcal{A}^{SS}_S$	χ^2/d.o.f.
HYP1	0.006	0.4293(22)	0.809(17)e + 4	0.1280(24)e + 10	0.1168(26)e + 7	0.8	0.480(34)e + 1	0.6	−0.297(15)e + 1	0.8
	0.027	0.4530(15)	0.943(13)e + 4	0.1381(17)e + 10	0.1290(18)e + 7	0.9	0.387(12)e + 1	0.9	−0.2379(71)e + 1	0.4
	0.03	0.4557(15)	0.957(13)e + 4	0.1390(17)e + 10	0.1301(18)e + 7	1.0	0.374(11)e + 1	1.0	−0.2301(67)e + 1	0.4
HYP2	0.006	0.3855(19)	0.708(12)e + 4	0.1256(21)e + 10	0.1148(22)e + 7	0.8	0.1019(48)e + 2	0.3	−0.648(26)e + 1	0.2
	0.027	0.4114(14)	0.834(11)e + 4	0.1378(17)e + 10	0.1288(17)e + 7	1.7	0.792(20)e + 1	0.5	−0.500(12)e + 1	0.3
	0.03	0.4143(14)	0.846(11)e + 4	0.1388(16)e + 10	0.1301(16)e + 7	1.7	0.764(19)e + 1	0.5	−0.483(12)e + 1	0.3

(Table continued)

TABLE V. *(Continued)*

32c3, $m_h = 0.030$, $m_l = 0.008$

Smear	m_q	E_0	$\mathcal{A}^{\tilde{L}S}$	$\mathcal{A}^{\tilde{S}S}$	$\mathcal{A}^{SS}$	$\chi^2/\text{d.o.f.}$	$\mathcal{A}^{SS}_L$	$\chi^2/\text{d.o.f.}$	$\mathcal{A}^{SS}_S$	$\chi^2/\text{d.o.f.}$
HYP1	0.008	0.4296(24)	0.795(17)e + 4	0.1232(24)e + 10	0.1135(25)e + 7	0.7	0.491(37)e + 1	2.1	−0.285(18)e + 1	2.6
	0.027	0.4529(17)	0.924(15)e + 4	0.1337(20)e + 10	0.1258(21)e + 7	0.8	0.378(18)e + 1	1.8	−0.2261(95)e + 1	1.6
	0.03	0.4567(17)	0.943(14)e + 4	0.1349(19)e + 10	0.1275(21)e + 7	0.8	0.361(16)e + 1	1.8	−0.2164(88)e + 1	1.5
HYP2	0.008	0.3895(23)	0.717(14)e + 4	0.1247(22)e + 10	0.1141(24)e + 7	1.8	0.958(51)e + 1	1.2	−0.605(31)e + 1	1.6
	0.027	0.4126(16)	0.827(11)e + 4	0.1351(17)e + 10	0.1268(19)e + 7	1.8	0.739(28)e + 1	1.5	−0.465(17)e + 1	2.0
	0.03	0.4164(15)	0.843(11)e + 4	0.1363(16)e + 10	0.1284(18)e + 7	1.8	0.704(25)e + 1	1.5	−0.444(16)e + 1	1.9

The NLO SU(2)χPT formula for the B_d and B_s quantities ($\mathcal{Q}_{B_d}$ and $\mathcal{Q}_{B_s}$, respectively) with a unitary d quark is generally written as

$$\mathcal{Q}_{B_d} = \mathcal{Q}_0^{\mathrm{SU(2)}}\Bigg(1 + X_{\mathcal{Q}}\frac{Y_{\mathcal{Q}} + Z_{\mathcal{Q}}(g_{B^*B_\pi}^{\mathrm{SU(2)}})^2}{(4\pi f^{\mathrm{SU(2)}})^2}\ell(m_{LL}^2) + C_{\mathcal{Q}l}^{\mathrm{SU(2)}} m_{LL}^2 + C_{\mathcal{Q}h}^{\mathrm{SU(2)}}(m_{HH}^2 - m_{\mathrm{HH,phys}}^2) + C_{\mathcal{Q}a}^{\mathrm{SU(2)}} a^2\Bigg), \tag{126}$$

$$\mathcal{Q}_{B_s} = \mathcal{Q}_0^{(s)}(1 + C_{\mathcal{Q}l}^{(\mathrm{s})} m_{LL}^2 + C_{\mathcal{Q}h}^{(\mathrm{s})}(m_{HH}^2 - m_{\mathrm{HH,phys}}^2) + C_{\mathcal{Q}s}^{(\mathrm{s})}(m_{SS}^2 - m_{\mathrm{HH,phys}}^2) + C_{\mathcal{Q}a}^{(\mathrm{s})} a^2), \tag{127}$$

where

$$\ell(m_{LL}^2) = m_{LL}^2 \ln\left(\frac{m_{LL}^2}{\Lambda_\chi^2}\right), \tag{128}$$

$$m_{LL}^2 = 2B_0^{\mathrm{SU(2)}}(m_l + m_{\mathrm{res}}), \tag{129}$$

$$m_{HH}^2 = 2B_0^{\mathrm{SU(2)}}(m_h + m_{\mathrm{res}}), \tag{130}$$

$$m_{SS}^2 = 2B_0^{\mathrm{SU(2)}}(m_s + m_{\mathrm{res}}), \tag{131}$$

$$m_{\mathrm{HH,phys}}^2 = 2B_0^{\mathrm{SU(2)}}(m_h^{\mathrm{phys}} + m_{\mathrm{res}}), \tag{132}$$

with m_l, m_h, and m_s depicting unitary degenerate u and d, sea s and valence s-quark masses, respectively. $X_{\mathcal{Q}}$, $Y_{\mathcal{Q}}$, and $Z_{\mathcal{Q}}$ are constants that are specific to each physical quantity, and are given in Table VIII. $f^{\mathrm{SU(2)}}$, $B_0^{\mathrm{SU(2)}}$, $g_{B^*B_\pi}^{\mathrm{SU(2)}}$, $\mathcal{Q}_0^{\mathrm{SU(2)}}$, $C_{\mathcal{Q}l}^{\mathrm{SU(2)}}$, $C_{\mathcal{Q}h}^{\mathrm{SU(2)}}$, $C_{\mathcal{Q}a}^{\mathrm{SU(2)}}$, $\mathcal{Q}_0^{(\mathrm{s})}$, $C_{\mathcal{Q}l}^{(\mathrm{s})}$, $C_{\mathcal{Q}h}^{(\mathrm{s})}$, $C_{\mathcal{Q}s}^{(\mathrm{s})}$, and $C_{\mathcal{Q}a}^{(\mathrm{s})}$ are LECs. Note that these LECs are specific to SU(2)χPT, in which the effects of the s quark are integrated out at the physical s-quark mass m_h^{phys}. The s-quark mass dependence needs to be included, unless the s-quark mass has a physical value. It can be implemented by Taylor expansion of the LECs around the physical s-quark mass, as shown in Eqs. (126) and (127). In this work, we use two kinds of link smearing in the static quark action. Only the coefficients in front of a^2 are dependent on the smearing. We mention here that, because the B parameters express how the VSA holds well, its quark-mass dependence is expected to be mild. In fact, the logarithm in the χPT formula for B_B is suppressed for $g_{B^*B\pi} = 0.449$ [44] used in this study, which leads to a smaller coefficient of the logarithm term compared to that of the decay constant and matrix element. For the SU(3)-breaking ratios, the expression up to NLO becomes

TABLE VI. Correlator fit results [$O(a)$ improved].

24c1, $m_h = 0.040$, $m_l = 0.005$								
Smear	m_q	E_0	$\mathcal{A}^{\tilde{L}S}$	$\mathcal{A}^{\tilde{S}S}$	$\mathcal{A}^{SS}$	χ^2/d.o.f.	$\mathcal{A}_L^{SS}$	χ^2/d.o.f.
HYP1	0.005	0.5107(27)	0.1337(34)e + 5	0.1387(32)e + 10	0.2664(65)e + 7	1.3	0.311(13)e + 2	0.4
	0.034	0.5440(13)	0.1600(18)e + 5	0.1512(15)e + 10	0.2984(40)e + 7	1.4	0.2372(45)e + 2	0.6
	0.04	0.5510(12)	0.1650(17)e + 5	0.1531(14)e + 10	0.3037(38)e + 7	1.4	0.2198(38)e + 2	0.6
HYP2	0.005	0.4654(22)	0.1183(24)e + 5	0.1405(27)e + 10	0.2668(55)e + 7	1.3	0.559(16)e + 2	0.4
	0.034	0.4997(10)	0.1406(13)e + 5	0.1542(14)e + 10	0.3041(33)e + 7	2.1	0.4187(68)e + 2	0.3
	0.04	0.5072(10)	0.1450(13)e + 5	0.1564(13)e + 10	0.3098(31)e + 7	2.2	0.3858(59)e + 2	0.3
24c2, $m_h = 0.040$, $m_l = 0.01$								
Smear	m_q	E_0	$\mathcal{A}^{\tilde{L}S}$	$\mathcal{A}^{\tilde{S}S}$	$\mathcal{A}^{SS}$	χ^2/d.o.f.	$\mathcal{A}_L^{SS}$	χ^2/d.o.f.
HYP1	0.01	0.5118(35)	0.1339(43)e + 5	0.1371(41)e + 10	0.276(10)e + 7	1.8	0.318(16)e + 2	0.9
	0.034	0.5409(21)	0.1552(30)e + 5	0.1477(27)e + 10	0.3046(68)e + 7	1.8	0.2438(76)e + 2	1.1
	0.04	0.5481(19)	0.1601(28)e + 5	0.1496(25)e + 10	0.3098(64)e + 7	1.8	0.2255(66)e + 2	1.1
HYP2	0.01	0.4647(29)	0.1155(31)e + 5	0.1354(35)e + 10	0.2710(81)e + 7	0.9	0.600(21)e + 2	1.1
	0.034	0.4956(17)	0.1344(21)e + 5	0.1479(22)e + 10	0.3003(53)e + 7	1.1	0.439(10)e + 2	0.9
	0.04	0.5034(15)	0.1388(21)e + 5	0.1503(21)e + 10	0.3063(50)e + 7	1.1	0.4028(90)e + 2	0.9
32c1, $m_h = 0.030$, $m_l = 0.004$								
Smear	m_q	E_0	$\mathcal{A}^{\tilde{L}S}$	$\mathcal{A}^{\tilde{S}S}$	$\mathcal{A}^{SS}$	χ^2/d.o.f.	$\mathcal{A}_L^{SS}$	χ^2/d.o.f.
HYP1	0.004	0.4232(28)	0.775(19)e + 4	0.1197(29)e + 10	0.1107(31)e + 7	0.4	0.505(45)e + 1	0.5
	0.027	0.4519(14)	0.953(12)e + 4	0.1342(16)e + 10	0.1263(21)e + 7	0.6	0.399(16)e + 1	0.9
	0.03	0.4557(14)	0.973(12)e + 4	0.1355(15)e + 10	0.1279(21)e + 7	0.7	0.382(14)e + 1	1.0
HYP2	0.004	0.3818(28)	0.704(17)e + 4	0.1200(27)e + 10	0.1098(28)e + 7	1.0	0.1131(76)e + 2	2.0
	0.027	0.4116(14)	0.869(10)e + 4	0.1363(15)e + 10	0.1278(19)e + 7	1.4	0.867(23)e + 1	2.3
	0.03	0.4155(13)	0.887(10)e + 4	0.1377(15)e + 10	0.1295(19)e + 7	1.4	0.826(21)e + 1	2.3
32c2, $m_h = 0.030$, $m_l = 0.006$								
Smear	m_q	E_0	$\mathcal{A}^{\tilde{L}S}$	$\mathcal{A}^{\tilde{S}S}$	$\mathcal{A}^{SS}$	χ^2/d.o.f.	$\mathcal{A}_L^{SS}$	χ^2/d.o.f.
HYP1	0.006	0.4291(21)	0.830(17)e + 4	0.1277(24)e + 10	0.1166(26)e + 7	0.8	0.506(35)e + 1	0.7
	0.027	0.4528(15)	0.969(14)e + 4	0.1379(17)e + 10	0.1288(18)e + 7	0.9	0.409(13)e + 1	1.2
	0.03	0.4556(14)	0.984(13)e + 4	0.1387(16)e + 10	0.1299(17)e + 7	1.0	0.396(12)e + 1	1.3
HYP2	0.006	0.3853(18)	0.737(13)e + 4	0.1253(20)e + 10	0.1147(22)e + 7	0.8	0.1114(50)e + 2	0.4
	0.027	0.4113(14)	0.871(12)e + 4	0.1376(16)e + 10	0.1288(16)e + 7	1.8	0.860(22)e + 1	0.5
	0.03	0.4142(14)	0.884(12)e + 4	0.1386(16)e + 10	0.1301(16)e + 7	1.8	0.830(20)e + 1	0.5
32c3, $m_h = 0.030$, $m_l = 0.008$								
Smear	m_q	E_0	$\mathcal{A}^{\tilde{L}S}$	$\mathcal{A}^{\tilde{S}S}$	$\mathcal{A}^{SS}$	χ^2/d.o.f.	$\mathcal{A}_L^{SS}$	χ^2/d.o.f.
HYP1	0.008	0.4296(23)	0.818(17)e + 4	0.1233(24)e + 10	0.1135(25)e + 7	0.7	0.513(37)e + 1	1.9
	0.027	0.4529(17)	0.952(15)e + 4	0.1338(19)e + 10	0.1259(21)e + 7	0.8	0.399(18)e + 1	1.6
	0.03	0.4567(16)	0.972(15)e + 4	0.1350(19)e + 10	0.1275(20)e + 7	0.8	0.381(17)e + 1	1.6
HYP2	0.008	0.3895(22)	0.748(14)e + 4	0.1247(21)e + 10	0.1142(23)e + 7	1.7	0.1035(53)e + 2	1.3
	0.027	0.4127(15)	0.865(12)e + 4	0.1351(16)e + 10	0.1269(19)e + 7	1.7	0.804(29)e + 1	1.5
	0.03	0.4164(15)	0.882(11)e + 4	0.1364(16)e + 10	0.1285(18)e + 7	1.7	0.766(27)e + 1	1.5

$$\frac{\mathcal{Q}_{B_s}}{\mathcal{Q}_{B_d}} = \tilde{\mathcal{Q}}_0^{\mathrm{SU(2)}}\bigg(1 - X_{\mathcal{Q}}\frac{Y_{\mathcal{Q}} + Z_{\mathcal{Q}}(g_{B^*B_\pi}^{\mathrm{SU(2)}})^2}{(4\pi f^{\mathrm{SU(2)}})^2}\ell(m_{LL}^2) + \tilde{C}_{\mathcal{Q}l}^{\mathrm{SU(2)}} m_{LL}^2 + \tilde{C}_{\mathcal{Q}h}^{\mathrm{SU(2)}}(m_{HH}^2 - m_{\mathrm{HH,phys}}^2) + C_{\mathcal{Q}s}^{(\mathrm{s})}(m_{SS}^2 - m_{\mathrm{HH,phys}}^2) + \tilde{C}_{\mathcal{Q}a}^{\mathrm{SU(2)}} a^2\bigg). \qquad (133)$$

Note that these expressions do not give unity even at the $m_l = m_s$ point because SU(3) flavor symmetry is lost, and the SU(2)χPT formula can be applied only for the region $m_l \ll m_s$.

B. Details of the chiral fitting

For the chiral fit, we use the values of $f^{\mathrm{SU(2)}}$ and $B_0^{\mathrm{SU(2)}}$ from Ref. [26] and that of $g_{B^*B_\pi}^{\mathrm{SU(2)}}$ from Ref. [44], which are summarized in Table IX.

We carry out combined fits using HYP1 and HYP2 link-smearing data assuming that terms unrelated to the lattice spacing are common among the smearings. Their correlation is taken into account. As mentioned in the previous subsection, we introduce an s-quark mass dependence up to the linear term. To fully track the sea s-quark dependence, however, at least three independent data in the (m_h, a)

TABLE VII. Decay constants, matrix elements, and B parameters in lattice units at the simulation points. Φ_{B_s}, Φ_{B_s}/Φ_B, M_{B_s}, $(M_{B_s}/M_B)^{1/2}$, B_{B_s}, and $(B_{B_s}/B_B)^{1/2}$ are interpolated to the physical s quark mass. Matching factors are multiplied.

HYP1, $O(a)$ unimproved

Vol	m_l	Φ_B	Φ_{B_s}	Φ_{B_s}/Φ_B	M_B	M_{B_s}	$(M_{B_s}/M_B)^{1/2}$	B_B	B_{B_s}	$(B_{B_s}/B_B)^{1/2}$
24c	0.005	0.2613(38)	0.2998(21)	1.147(12)	0.1580(86)	0.2098(56)	1.152(22)	0.867(38)	0.875(17)	1.004(15)
24c	0.01	0.2630(48)	0.2940(33)	1.118(11)	0.158(10)	0.1986(74)	1.118(20)	0.861(42)	0.861(23)	1.000(15)
32c	0.004	0.1611(22)	0.1872(15)	1.162(12)	0.568(49)	0.788(29)	1.178(42)	0.820(67)	0.843(28)	1.014(34)
32c	0.006	0.1674(20)	0.1880(16)	1.1230(71)	0.625(44)	0.808(30)	1.136(28)	0.837(56)	0.857(26)	1.012(24)
32c	0.008	0.1676(20)	0.1873(17)	1.1179(73)	0.658(49)	0.806(38)	1.107(25)	0.879(59)	0.861(35)	0.990(19)

HYP2, $O(a)$ unimproved

Vol	m_l	Φ_B	Φ_{B_s}	Φ_{B_s}/Φ_B	M_B	M_{B_s}	$(M_{B_s}/M_B)^{1/2}$	B_B	B_{B_s}	$(B_{B_s}/B_B)^{1/2}$
24c	0.005	0.2327(27)	0.2638(15)	1.134(10)	0.1193(49)	0.1555(34)	1.142(17)	0.825(26)	0.837(14)	1.007(11)
24c	0.01	0.2312(35)	0.2573(23)	1.113(10)	0.1237(57)	0.1521(44)	1.109(14)	0.867(30)	0.861(18)	0.996(10)
32c	0.004	0.1483(20)	0.1718(12)	1.158(11)	0.491(33)	0.670(23)	1.168(32)	0.837(51)	0.851(24)	1.008(25)
32c	0.006	0.1522(15)	0.1713(14)	1.1256(69)	0.505(24)	0.652(20)	1.136(18)	0.817(35)	0.833(20)	1.010(15)
32c	0.008	0.1547(18)	0.1716(14)	1.1093(72)	0.525(25)	0.637(21)	1.102(16)	0.822(35)	0.811(23)	0.993(11)

HYP1, $O(a)$ improved

Vol	m_l	Φ_B	Φ_{B_s}	Φ_{B_s}/Φ_B	M_B	M_{B_s}	$(M_{B_s}/M_B)^{1/2}$	B_B	B_{B_s}	$(B_{B_s}/B_B)^{1/2}$
24c	0.005	0.2706(38)	0.3112(21)	1.150(12)	0.1661(89)	0.2217(58)	1.156(22)	0.850(36)	0.858(17)	1.005(15)
24c	0.01	0.2726(49)	0.3053(34)	1.120(11)	0.167(10)	0.2105(77)	1.120(20)	0.846(40)	0.846(22)	1.000(14)
32c	0.004	0.1658(22)	0.1928(15)	1.163(12)	0.593(50)	0.824(30)	1.178(41)	0.809(65)	0.831(28)	1.013(33)
32c	0.006	0.1720(20)	0.1935(17)	1.1252(71)	0.654(44)	0.847(31)	1.138(28)	0.829(54)	0.848(25)	1.011(23)
32c	0.008	0.1724(21)	0.1930(17)	1.1196(72)	0.686(49)	0.845(39)	1.110(24)	0.865(57)	0.850(34)	0.991(18)

HYP2, $O(a)$ improved

Vol	m_l	Φ_B	Φ_{B_s}	Φ_{B_s}/Φ_B	M_B	M_{B_s}	$(M_{B_s}/M_B)^{1/2}$	B_B	B_{B_s}	$(B_{B_s}/B_B)^{1/2}$
24c	0.005	0.2450(28)	0.2791(15)	1.139(10)	0.1295(52)	0.1699(37)	1.145(17)	0.809(25)	0.818(13)	1.006(10)
24c	0.01	0.2439(36)	0.2724(24)	1.1166(98)	0.1348(61)	0.1664(47)	1.111(13)	0.849(28)	0.840(17)	0.9950(96)
32c	0.004	0.1547(20)	0.1795(13)	1.160(11)	0.530(34)	0.717(24)	1.163(31)	0.830(48)	0.834(23)	1.002(23)
32c	0.006	0.1585(16)	0.1790(15)	1.1292(69)	0.545(25)	0.701(21)	1.134(17)	0.813(33)	0.820(19)	1.004(14)
32c	0.008	0.1614(18)	0.1796(15)	1.1124(72)	0.562(27)	0.687(23)	1.106(16)	0.809(34)	0.799(22)	0.994(11)

parameter space are required. Our simulation setting only has one sea s-quark mass parameter for each lattice spacing and the parameter is not tuned to the physical one, and therefore the data cannot be fitted using the formulas (126), (127), and (133). Nevertheless, we use these formulas assuming that the sea s-quark mass parameter is on the physical point, which causes the sea s-quark terms to vanish. Later on we estimate the uncertainty from this inconsistency using partially quenched SU(3)χPT. On the other hand, we have two valence s-quark mass data points. In our analysis we first linearly interpolate the data to the physical s quark mass point using the two valence data points, and then the fit functions are applied by setting $m_s = m_h^{\mathrm{phys}}$.

In order to take into account the ambiguity of the chiral fit function ansatz, we also use a linear fit function form,

$$\mathcal{G}(m_L, a) = \mathcal{G}_0(1 + C'_l m_{LL}^2 + C'_a a^2), \tag{134}$$

for B_d quantities and SU(3)-breaking ratios, which has the same form as that for the B_s sector in the SU(2)χPT

TABLE VIII. Constants X_Q, Y_Q, and Z_Q in Eqs. (126) and (133).

$\mathcal{Q}$	$X_\mathcal{Q}$	$Y_\mathcal{Q}$	$Z_\mathcal{Q}$
Φ	$-3/4$	1	3
M	-1	2	3
B	$-1/2$	1	-3

TABLE IX. Low-energy constants used in this work.

LECs	NLO SU(2)χPT	NLO SU(2)χPT(FV)
$B_0^{\mathrm{SU}(2)}$ [GeV] [26]	4.12(7)	4.03(7)
$f^{\mathrm{SU}(2)}$ [GeV] [26]	0.110(2)	0.112(2)
$g_{B^*B_\pi}^{\mathrm{SU}(2)}$ [44]	$0.449(47)_{\mathrm{stat}}(19)_{\mathrm{sys}}$	
Λ_χ [GeV]	1.0	

TABLE X. Chiral fit results in lattice units using the SU(2)χPT formula. The values show physical-point and continuum-limit results. Matching factors are multiplied.

	HYP1				HYP2				Combined			
	$O(a)$-unimp		$O(a)$-imp		$O(a)$-unimp		$O(a)$-imp		$O(a)$-unimp		$O(a)$-imp	
	Value	χ^2/d.o.f.	Value	χ^2/d.o.f.	Value	χ^2/d.o.f.	Value	χ^2/d.o.f.	Value	χ^2/d.o.f.	Value	χ^2/d.o.f.
Φ_B	0.1437(50)	0.78	0.1460(50)	0.67	0.1400(41)	1.17	0.1436(42)	1.06	0.1392(41)	2.00	0.1428(42)	1.51
Φ_{B_s}	0.1766(37)	0.77	0.1795(38)	0.75	0.1725(30)	1.27	0.1771(31)	1.36	0.1726(31)	2.18	0.1772(32)	1.30
Φ_{B_s}/Φ_B	1.228(23)	0.74	1.229(22)	0.66	1.236(20)	0.33	1.238(20)	0.22	1.233(20)	0.74	1.235(20)	0.69
M_B	0.432(91)	0.37	0.443(93)	0.34	0.410(50)	0.03	0.435(52)	0.01	0.402(50)	0.36	0.430(54)	0.33
M_{B_s}	0.686(64)	0.68	0.704(67)	0.70	0.653(40)	0.09	0.683(43)	0.04	0.636(39)	1.03	0.669(41)	0.86
$\sqrt{M_{B_s}/M_B}$	1.261(62)	0.07	1.261(61)	0.05	1.262(42)	0.19	1.255(41)	0.06	1.262(43)	0.08	1.255(42)	0.04
B_B	0.79(11)	0.20	0.79(11)	0.17	0.753(74)	0.34	0.763(70)	0.42	0.757(78)	0.57	0.766(75)	0.62
B_{B_s}	0.833(53)	0.20	0.829(52)	0.22	0.807(40)	1.23	0.802(38)	1.09	0.804(41)	1.56	0.802(39)	1.45
$\sqrt{B_{B_s}/B_B}$	1.019(45)	0.19	1.020(44)	0.15	1.025(30)	0.13	1.018(29)	0.05	1.023(31)	0.09	1.016(29)	0.09

framework. We also investigate the uncertainty from chiral fits by eliminating the heaviest quark mass data in both the 24c and 32c ensembles.

C. Scaling check and $O(a)$ improvement

We present fit results using the SU(2)χPT formula in Table X. We also show the chiral fit using the SU(2)χPT formula in Figs. 1 and 2, in which both $O(a)$-unimproved and -improved results are presented. The features of the data are as follows.

(i) The data shows that HYP1 smearing gives larger scaling violations than HYP2.

(ii) HYP1 and HYP2 results are almost consistent with each other in the continuum limit. This consistency is seen even in the $O(a)$-unimproved case within large statistical errors. While the $O(a)$-improved data shows slightly better consistency than the unimproved case, we cannot see any clear effectiveness of the $O(a)$-improvement with the current statistics.

(iii) The $O(a)$ improvement slightly pushes data up for decay constants and matrix elements at each simulation point.

(iv) Being a ratio, the scaling violation for ξ and f_{B_s}/f_B is tiny. HYP1 and HYP2 $O(a)$-improved and -unimproved results are consistent at each simulation point.

When $O(a)$ improvement is successfully accomplished and a^2 scaling is used in the continuum extrapolation [assuming that the $O(\alpha_s^2 a)$ and $O(a^3)$ contributions are small], HYP1 and HYP2 results must give the same value in the continuum limit, and our data is actually consistent with this observation. Therefore we use a combined fit of HYP1 and HYP2 assuming that the chiral fit parameter for each smearing is different only for the coefficients of the a^2 term.

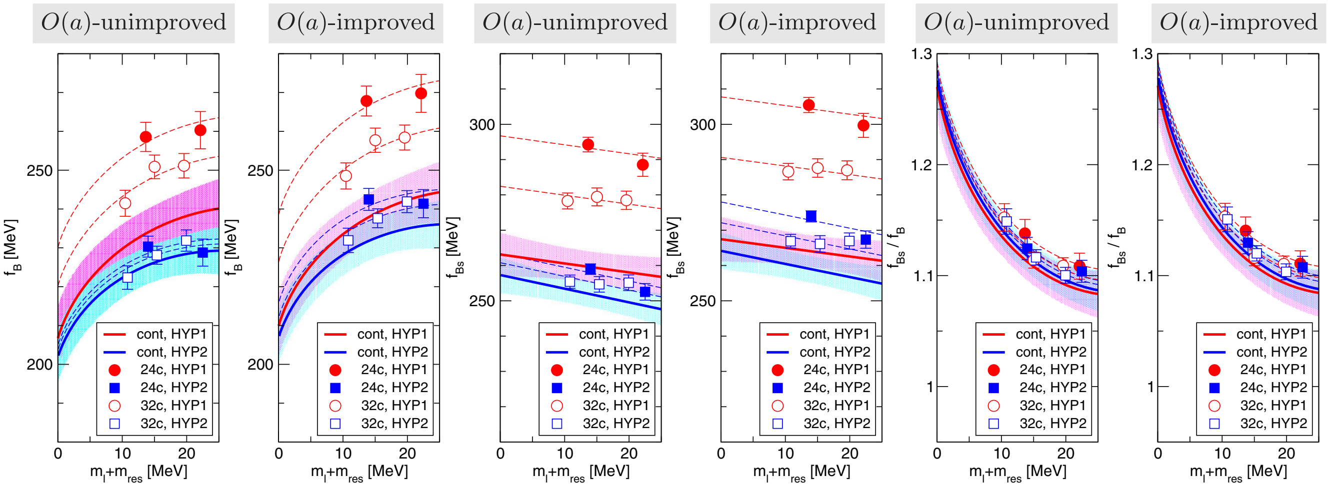

FIG. 1 (color online). The SU(2)χPT fit of f_B, f_{B_s}, and f_{B_s}/f_B comparing $O(a)$-unimproved and -improved data. HYP1 and HYP2 data are fit independently. Thick lines with bands represent the continuum limit.

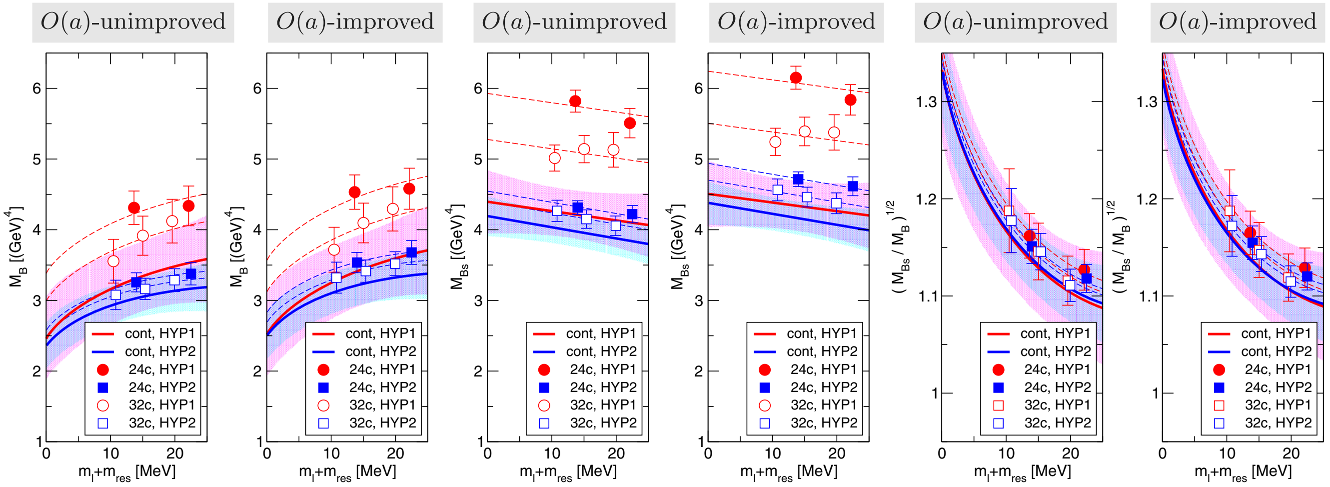

FIG. 2 (color online). The SU(2)χPT fit of $\mathcal{M}_B$, $\mathcal{M}_{B_s}$, and $\sqrt{\mathcal{M}_{B_s}/\mathcal{M}_B}$ comparing $O(a)$-unimproved and -improved data. HYP1 and HYP2 data are fit independently. Thick lines with bands represent the continuum limit.

D. Fit results and criteria for final results

In this work, $O(a)$-improved data are taken for the final results. Hereafter, numerical data and figures indicate the $O(a)$-improved case. We present chiral fit results in Figs. 3, 4, and 5. Correlations between the two kinds of link smearing in the static action is included in the fitting. χ^2/d.o.f.'s and p values in the fits are presented in the figures. the χ^2/d.o.f.'s in each fit are all at an acceptable level, and thus it is hard to exclude any of the fit using the ansatz. We thus take the following criteria for the chiral and continuum extrapolations.

(i) For B_d quantities and SU(3)-breaking ratios, an average of the results from SU(2)χPT and the linear fit, whose physical point values are presented in Table XI, is taken. We then take half of the full difference between the SU(2)χPT and linear results as an uncertainty from the chiral fit function ansatz.

(ii) For B_s quantities, the SU(2)χPT fit (linear fit) results are taken as central values. To investigate the chiral fit form ambiguity, data in the region $m_\pi >$ 350 MeV are removed and we see its effect on the extrapolated value. We take the difference between the full data and cut data—where the heaviest quark mass points at each lattice spacing are removed ("SU(2)χPT cut" in Figs. 3, 4, and 5)—as a chiral fit ambiguity.

Combined with the ratio of the decay constants, ξ can be obtained from Eq. (20). While the ratio of the B parameters is well determined, the current data for the decay constants

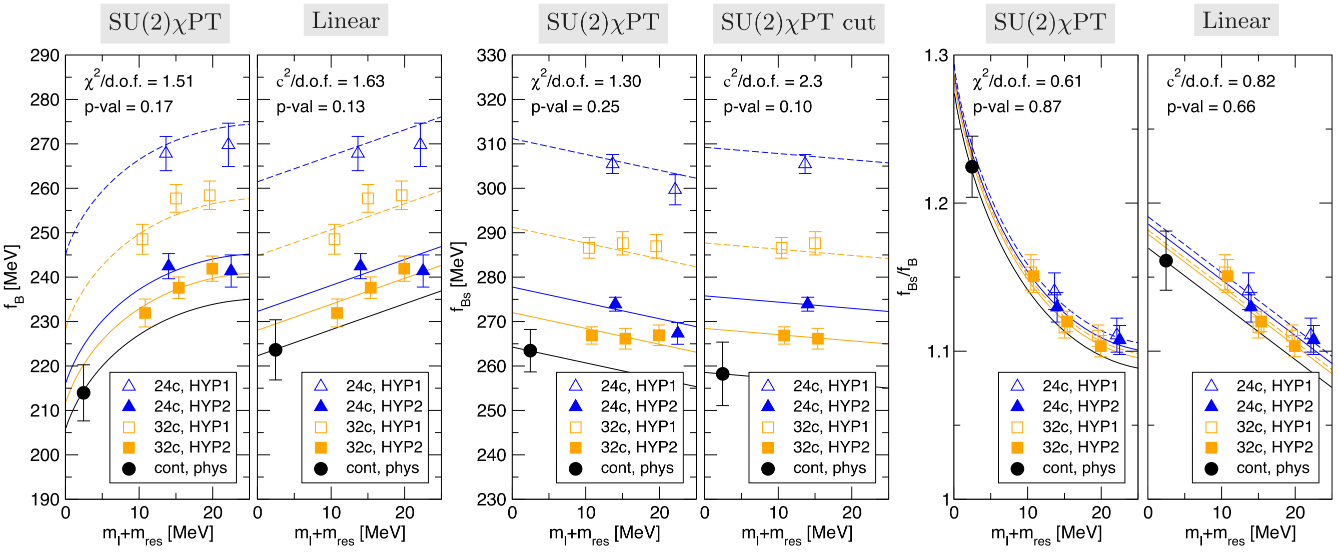

FIG. 3 (color online). Chiral fit of f_B, f_{B_s}, and f_{B_s}/f_B using the SU(2)χPT and linear formulas. "cut" indicates that the heaviest quark mass points at each lattice spacing were removed in the fitting.

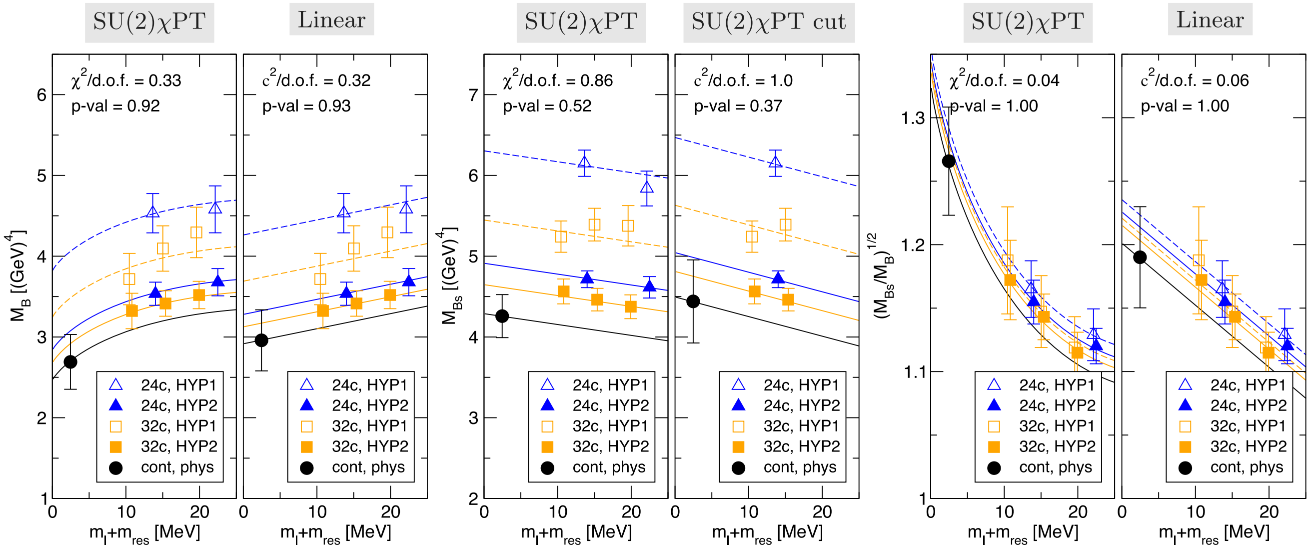

FIG. 4 (color online). Chiral fit of $\mathcal{M}_B$, $\mathcal{M}_{B_s}$, and $(\mathcal{M}_{B_s}/\mathcal{M}_B)^{1/2}$ using the SU(2)χPT and linear formulas. “cut” indicates that the heaviest quark mass points at each lattice spacing were removed in the fitting.

has a large uncertainty from the chiral extrapolation, which also leads to a poor determination of ξ from Eq. (20) and does not provide any gain. We hence simply use Eq. (3) to calculate ξ in this work.

E. Finite-volume effect

Our lattice has a modest physical volume of around 2.75 fm and the lowest $m_\pi L$ is about 4; thus, we may estimate the FV uncertainty using FV NLOχPT. The FV correction can be included in the χPT formula by replacing the chiral logarithms (128) with [45,46]

$$\ell(m_{LL}^2) = m_{LL}^2 \ln\left(\frac{m_{LL}^2}{\Lambda_\chi^2} + \delta_1(m_{LL}L)\right), \qquad (135)$$

$$\delta_1(m_{LL}L) = \frac{4}{m_{LL}L}\sum_{\vec{r}\neq 0}\frac{K_1(|r|m_{LL}L)}{|r|}, \qquad (136)$$

where K_1 are modified Bessel functions of the second kind. For the numerical implementation of Eq. (136), we use the multiplicities given in Refs. [43,45]. With SU(2)χPT for the chiral extrapolation, we cannot

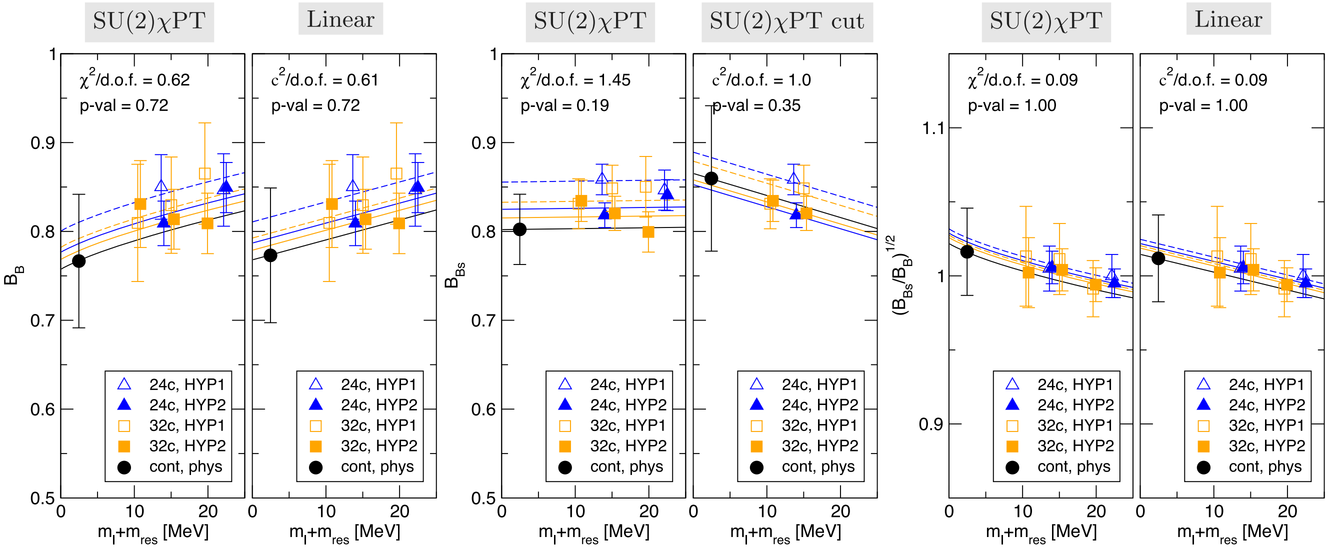

FIG. 5 (color online). Chiral fit of B_B, B_{B_s}, and $(B_{B_s}/B_B)^{1/2}$ using the SU(2)χPT and linear formulas. “cut” indicates that the heaviest quark mass points at each lattice spacing were removed in the fitting.

TABLE XI. Chiral fit results in lattice units using the linear fit function. The values show physical-point and continuum-limit results. Matching factors are multiplied.

	HYP1				HYP2				Combined			
	$O(a)$-unimp		$O(a)$-imp		$O(a)$-unimp		$O(a)$-imp		$O(a)$-unimp		$O(a)$-imp	
	Value	χ^2/d.o.f.	Value	χ^2/d.o.f.	Value	χ^2/d.o.f.	Value	χ^2/d.o.f.	Value	χ^2/d.o.f.	Value	χ^2/d.o.f.
Φ_B	0.1500(53)	1.17	0.1523(54)	1.03	0.1463(44)	1.63	0.1501(46)	1.48	0.1455(44)	2.14	0.1492(45)	1.63
Φ_{B_s}	0.1766(37)	0.77	0.1795(38)	0.75	0.1725(30)	1.27	0.1771(31)	1.36	0.1726(31)	2.18	0.1772(32)	1.30
Φ_{B_s}/Φ_B	1.164(22)	1.37	1.165(21)	1.27	1.172(20)	1.01	1.174(19)	0.82	1.169(20)	1.00	1.171(19)	0.94
M_B	0.47(10)	0.44	0.48(10)	0.41	0.450(55)	0.03	0.477(58)	0.01	0.442(56)	0.36	0.472(60)	0.32
M_{B_s}	0.686(64)	0.68	0.704(67)	0.70	0.653(40)	0.09	0.683(43)	0.04	0.636(39)	1.03	0.669(41)	0.86
$\sqrt{M_{B_s}/M_B}$	1.186(58)	0.16	1.187(57)	0.13	1.186(40)	0.29	1.180(38)	0.12	1.187(40)	0.12	1.180(39)	0.06
B_B	0.80(11)	0.20	0.80(11)	0.17	0.760(75)	0.33	0.769(71)	0.41	0.763(79)	0.57	0.773(75)	0.61
B_{B_s}	0.833(53)	0.20	0.829(52)	0.22	0.807(40)	1.23	0.802(38)	1.09	0.804(41)	1.56	0.802(39)	1.45
$\sqrt{B_{B_s}/B_B}$	1.015(45)	0.19	1.015(44)	0.15	1.020(30)	0.13	1.013(28)	0.05	1.019(30)	0.09	1.012(29)	0.09

evaluate the FV effect for the B_s sector in this procedure. The effect is, however, expected to be quite small in this sector, and we estimate that this uncertainty is negligible. In the simulated quark-mass region, the FV correction slightly pushes the data up for B_d quantities, and hence it pushed them down for the SU(3)-breaking ratios, f_{B_s}/f_B and ξ.

VIII. SYSTEMATIC ERRORS

In this section we clarify the systematic errors we take into account. A summary of the systematic errors is shown in Table XII and also in Fig. 6.

A. Chiral extrapolation

As described in Sec. VII, we use the SU(2)χPT formula for the chiral and continuum extrapolations. The linear fit function ansatz cannot be excluded with the current statistics, and thus we take their average. The method for estimating the associated systematic errors has been described in detail in Sec. VII.

B. $g_{B^*B\pi}$

In the chiral fit, we use $g_{B^*B\pi} = 0.449(47)(19)$, where the first uncertainty is statistical and the second is systematic [44]. This value was obtained using the 2 + 1-flavor dynamical DWF configurations, which is the same as that used in this simulation. The systematic errors were fully evaluated in Ref. [44], and thus we quote this value as a reliable one. We use 0.449 as a central value and change it by ±0.051 in the chiral fit for the uncertainty of this coupling.

C. Discretization

The static heavy- and light-quark system has $O(a)$ lattice discretization errors even if chiral fermions are employed for the light quarks, in which case the $O(a)$ discretization errors start with $O(\alpha_s a)$. In this simulation, $O(a)$ improvement is made using one-loop perturbation theory [30]. Thus, the remaining $O(a)$ lattice artifact is supposed to be $O(\alpha_s^2 a)$ at each simulated lattice spacing a. For the lattice artifact, the coupling should be the lattice one, i.e., defined

TABLE XII. Error budget [%] for final quantities.

	f_B	f_{B_s}	f_{B_s}/f_B	$f_B\sqrt{\hat{B}_B}$	$f_{B_s}\sqrt{\hat{B}_{B_s}}$	ξ	$\hat{B}_B$	$\hat{B}_{B_s}$	B_{B_s}/B_B
Statistics	2.99	1.81	1.65	6.34	3.12	3.36	9.80	4.93	5.80
Chiral/continuum extrapolation	3.54	1.98	2.66	2.55	2.13	3.08	14.84	7.15	3.66
Finite-volume effect	0.82	0.0	1.00	0.76	0.00	1.07	0.15	0.0	0.16
Discretization	1.0	1.0	0.2	1.0	1.0	0.2	1.0	1.0	0.2
One-loop renormalization	6.0	6.0	0.0	6.0	6.0	1.2	6.0	6.0	1.2
$g_{B^*B\pi}$	0.24	0.00	0.35	0.14	0.00	0.25	0.20	0.00	0.22
Scale	1.82	1.85	0.04	1.84	1.86	0.05	0.04	0.05	0.02
Physical quark mass	0.05	0.01	0.06	0.06	0.19	0.20	0.03	0.00	0.02
Off-physical sea s-quark mass	0.84	0.69	0.79	0.20	0.39	0.91	0.28	0.19	0.42
Fit range	0.44	2.31	0.26	0.10	1.74	0.58	3.14	0.00	1.54
Total systematic error	7.38	7.09	3.00	6.90	6.94	3.66	16.34	9.39	4.18
Total error (incl. statistical)	7.96	7.32	3.42	9.37	7.61	4.97	19.05	10.61	7.15

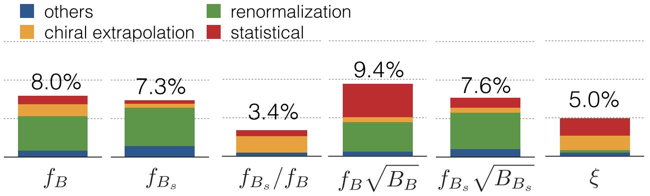

FIG. 6 (color online). Error budget for final quantities. The height of the bars denotes the total error, while the relative size of the colors is determined by the squared errors.

by Eq. (89), whose actual value is shown in Table III. Conservatively assuming $\Lambda_{\mathrm{QCD}} \sim 500$ MeV, the order of magnitude for each discretization error is summarized in Table XIII. While without one-loop perturbative $O(a)$ improvement the magnitude of the $O(\alpha_s a)$ term is more than half of the $O(a^2)$ term, the improvement reduces it substantially. The uncertainties from $O(\alpha_s^2 a)$ are ~0.9% (24c) and ~0.6% (32c). The uncertainty from the $O(a^3)$ contribution, which starts at the one-loop level, is even smaller than that. Thus we take 1% as an uncertainty from the remaining $O(a)$ and $O(a^3)$ contributions in the continuum. For the SU(3)-breaking ratios, the lattice artifact comes with a factor of $(m_s - m_d)/\Lambda_{\mathrm{QCD}} \sim 0.2$, which leads to a reduced uncertainty down of 0.2%.

D. Renormalization

In this work, renormalization is carried out in the one-loop perturbation framework. We use power counting to estimate the higher-order uncertainty of the perturbation. We use a two-step matching procedure: first, full QCD theory and HQET are matched in the continuum at a scale $\mu = m_b$; second, continuum and lattice HQET are matched at the scale $\mu = a^{-1}$. The values of α_s in these matchings are presented in Table XIII. Assuming that the coefficients of the power expansion are one, the counting estimation shows a two-loop uncertainty of 5.1% in the first matching and of 3.1% in the second. We add them in quadrature, leading to 6%. For the ratio of the decay constants, the renormalization factor is completely canceled out, and thus the perturbation ambiguity is negligible. For ξ, however, the nonvanishing contribution Z_2/Z_1 remains in the ratio, which causes an uncertainty. Nevertheless, because this uncertainty is suppressed by a factor of $(m_s - m_l)/\Lambda_{\mathrm{QCD}} \sim 0.2$, the one-loop ambiguity is reduced to 1.2%. We note that the one-loop perturbation ambiguity also exists in the $O(a)$ improvement coefficients, which is counted as the discretization error (as discussed the previous subsection).

TABLE XIII. Power counting for perturbation and discretization error estimations. We here define $\hat{a} = a\Lambda_{\mathrm{QCD}}$.

$\alpha_s(m_b)$	0.2261	
$(\alpha_s(m_b))^2$	0.0511	
	24c	32c
α_s^{LAT}	0.1769	0.1683
$(\alpha_s^{\mathrm{LAT}})^2$	0.0313	0.0283
$\hat{a}$	0.29	0.22
$\hat{a}^2$	0.084	0.048
$\hat{a}^3$	0.024	0.011
$\alpha_s^{\mathrm{LAT}}\hat{a}$	0.051	0.037
$(\alpha_s^{\mathrm{LAT}})^2\hat{a}$	0.0091	0.0062
$\alpha_s^{\mathrm{LAT}}\hat{a}^3$	0.0042	0.0019
$\hat{a}^2$: $\alpha_s^{\mathrm{LAT}}\hat{a}$: $\alpha_s^{\mathrm{LAT}}\hat{a}^3$	1 : 0.61 : 0.05	1 : 0.77 : 0.04
$\hat{a}^2$: $(\alpha_s^{\mathrm{LAT}})^2\hat{a}$: $\alpha_s^{\mathrm{LAT}}\hat{a}^3$	1 : 0.11 : 0.05	1 : 0.13 : 0.04

E. Scale

As shown in Table I, the lattice scales used in this study have a 1%-level uncertainty. We investigate the systematic error from this by varying the value of the lattice spacing within the uncertainty. While the matching factors and $O(a)$-improved coefficients need to be implicitly varied for this search, the effect is negligible. Thus we only take the error into account when the lattice units are converted into physical units and the chiral/continuum extrapolations are carried out.

F. Light-quark mass

Light-quark masses at the physical point also have a 3%-level uncertainty, as shown in Table IV. This affects the values of the physical observables. We check the effects by varying the physical quark-mass values within the uncertainty.

G. Of-physical sea *s*-quark mass

Our gluon ensemble has only one dynamical *s*-quark mass parameter, which is slightly off from the physical *s*-quark mass. In spite of this, we use the SU(2)χPT fit functions assuming that the sea *s* quark is at the physical mass. The uncertainty from this inconsistency must be investigated. To deal with it, we make an estimation using SU(3)χPT as a model. We use partially quenched SU(3)HMχPT [47,48], whose explicit formulas are also presented in Ref. [40]. The ambiguity from the off-physical *s*-quark mass effect is investigated by taking the difference between the correct treatment of our simulation setup and the fake treatment where the *s*-quark mass is assumed to be at the physical point.

H. Finite volume

The FV effect is estimated using FVχPT, as mentioned in Sec. VII. The uncertainty from the FV effect is estimated from the difference between SU(2)χPT and FV SU(2)χPT. The effect for B_s quantities is expected to be significantly small, and thus it is neglected in our analysis.

I. Fit-range dependence

As mentioned in Sec. VI E, our correlator fit results have a non-negligible fit-range dependence. Although this uncertainty is statistical rather than systematic, we count it as a systematic error here. To take into account the uncertainty of the fit range choices, we shift the minimal value of t in the fit range toward a larger value by 2 for the 2PT functions and shorten the range by 2 for the 3PT functions. In Appendix B, the physical quantities with the original and shifted fit ranges for each simulation parameter are shown in Figs. 16, 17, and 18. We find that non-negligible fit range dependencies remain in some cases; the cases in which the difference between the fit range choices is beyond 1σ statistical error are listed in the caption of each figure. We define the uncertainty of the fit range dependencies as follows.

1. When physical quantities at some quark-mass parameter move beyond 1σ statistical error by changing the fit range, the data at the mass parameter for both HYP1 and HYP2 are replaced to see the effect of the move.
2. Chiral/continuum fits are performed to investigate the shift caused by the replacement of the data.
3. We repeat this procedure for each data point that has a large shift beyond 1σ statistical error by changing the fit range.
4. The final uncertainty is obtained by adding each shift of the chiral/continuum extrapolated value in quadrature.

The resulting uncertainty is taken as a systematic error in our calculation.

IX. CONCLUSIONS

A. Results of physical quantities

We present the final results for B meson quantities in the static limit of the b quark:

$$[f_B]^{\rm static} = 218.8(6.5)_{\rm stat}(16.1)_{\rm sys}\ {\rm MeV}, \qquad (137)$$

$$[f_{B_s}]^{\rm static} = 263.5(4.8)_{\rm stat}(18.7)_{\rm sys}\ {\rm MeV}, \qquad (138)$$

$$[f_{B_s}/f_B]^{\rm static} = 1.193(20)_{\rm stat}(36)_{\rm sys}, \qquad (139)$$

$$\left[f_B\sqrt{\hat{B}_B}\right]^{\rm static} = 240(15)_{\rm stat}(17)_{\rm sys}\ {\rm MeV}, \qquad (140)$$

$$\left[f_{B_s}\sqrt{\hat{B}_{B_s}}\right]^{\rm static} = 290(09)_{\rm stat}(20)_{\rm sys}\ {\rm MeV}, \qquad (141)$$

$$[\xi]^{\rm static} = 1.208(41)_{\rm stat}(44)_{\rm sys}, \qquad (142)$$

$$[\hat{B}_B]^{\rm static} = 1.17(11)_{\rm stat}(19)_{\rm sys}, \qquad (143)$$

$$[\hat{B}_{B_s}]^{\rm static} = 1.22(06)_{\rm stat}(11)_{\rm sys}, \qquad (144)$$

$$[B_{B_s}/B_B]^{\rm static} = 1.028(60)_{\rm stat}(43)_{\rm sys}, \qquad (145)$$

where the first errors are statistical and the second are systematic. Note that the $O(1/m_b)$ uncertainty, which is mentioned in the next subsection, is not included in the systematic errors above. We also show final results including the $O(1/m_b)$ uncertainty in the systematic error:

$$f_B = 218.8(6.5)_{\rm stat}(30.8)_{\rm sys}\ {\rm MeV}, \qquad (146)$$

$$f_{B_s} = 263.5(4.8)_{\rm stat}(36.7)_{\rm sys}\ {\rm MeV}, \qquad (147)$$

$$f_{B_s}/f_B = 1.193(20)_{\rm stat}(44)_{\rm sys}, \qquad (148)$$

$$f_B\sqrt{\hat{B}_B} = 240(15)_{\rm stat}(33)_{\rm sys}\ {\rm MeV}, \qquad (149)$$

$$f_{B_s}\sqrt{\hat{B}_{B_s}} = 290(09)_{\rm stat}(40)_{\rm sys}\ {\rm MeV}, \qquad (150)$$

$$\xi = 1.208(41)_{\rm stat}(52)_{\rm sys}, \qquad (151)$$

$$\hat{B}_B = 1.17(11)_{\rm stat}(24)_{\rm sys}, \qquad (152)$$

$$\hat{B}_{B_s} = 1.22(06)_{\rm stat}(19)_{\rm sys}, \qquad (153)$$

$$B_{B_s}/B_B = 1.028(60)_{\rm stat}(49)_{\rm sys}. \qquad (154)$$

We present here the constraint on the ratio of the CKM matrix element (2) obtained through Eq. (12):

$$\left|\frac{V_{td}}{V_{ts}}\right| = 0.206(13), \qquad (155)$$

where the statistical and systematic errors including the $O(1/m_b)$ uncertainty are all added in quadrature.

B. Comparison with other approaches and the $1/m_b$ ambiguity

Since we use the static approximation for the b quark, there exists an $O(\Lambda_{\rm QCD}/m_b)$ uncertainty for the physical quantities. Here, we take the PDG value for the b-quark mass in the $\overline{\rm MS}$ scheme, $m_b = 4.18(03)$ GeV [15], and we assume $\Lambda_{\rm QCD} = 0.5$ GeV. The uncertainty from the static approximation becomes 12%. For the SU(3)-breaking ratios, however, there would be a suppression factor coming from the SU(3) light flavor symmetry, which leads to

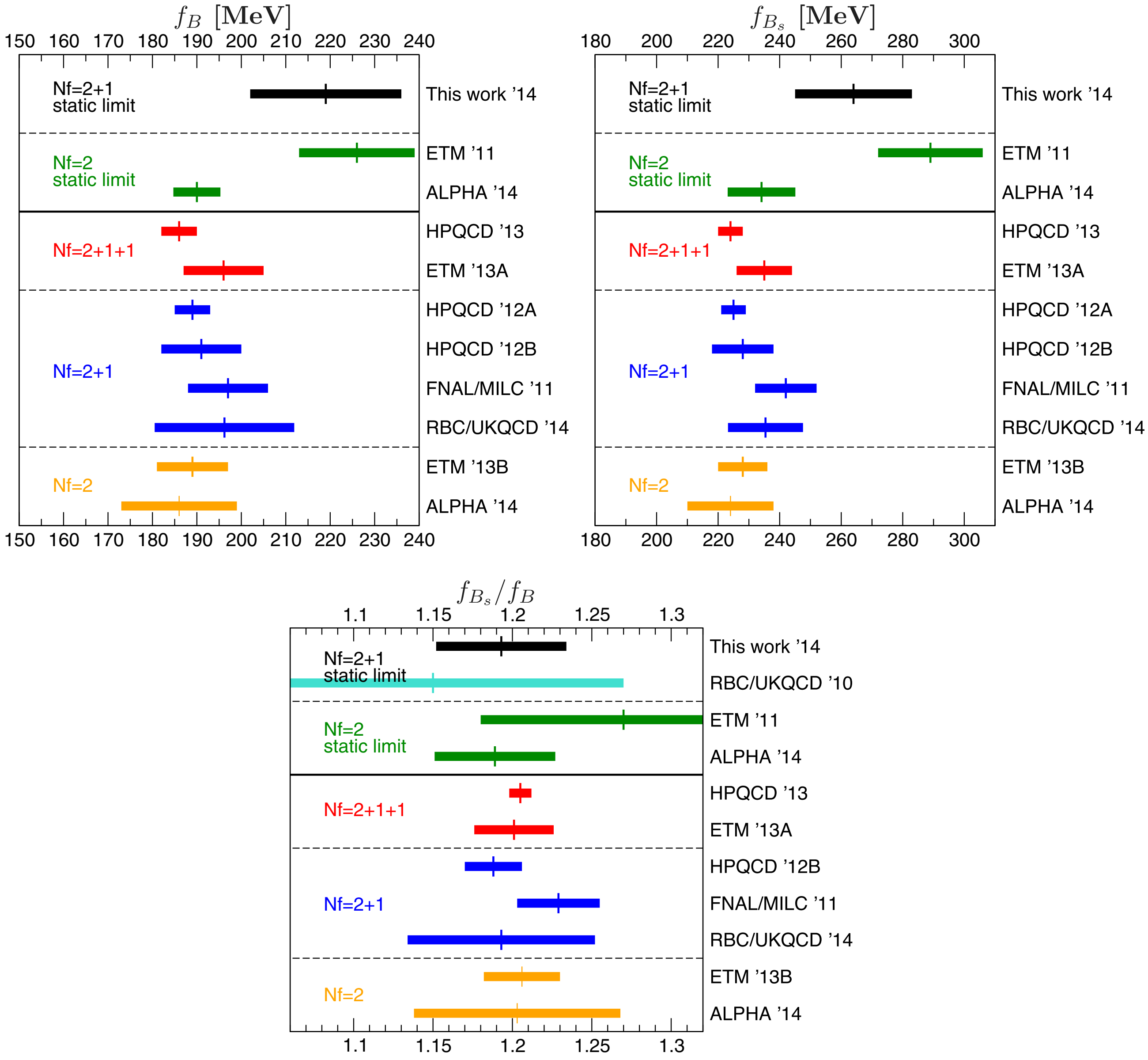

FIG. 7 (color online). Comparison of f_B, f_{B_s}, and f_{B_s}/f_B with other works. The data is cited from Refs. [50] (ETM 2011), [12] (ALPHA 2014), [51] (HPQCD 2013), [52] (ETM 2013A), [53,54] (HPQCD 2012A, HPQCD 2012B), [55] (FNAL/MILC 2011), [56] (RBC/UKQCD 2014), [14] (ETM 2013B), and [40] (RBC/UKQCD 2010). The values of f_B and f_{B_s} in ETM 2011 are obtained from Φ_B and Φ_{B_s} divided by $\sqrt{m_B}$ and $\sqrt{m_{B_s}}$, respectively. Errors for the static-limit results do not contain the $1/m_b$ uncertainty.

$$\frac{\Lambda_{\rm QCD}}{m_b} \times \frac{m_s - m_d}{\Lambda_{\rm QCD}} \sim 2.2\%. \tag{156}$$

We show comparisons with other works for our obtained quantities in Figs. 7, 8, and 9. (See also the review of lattice results by the Flavor Lattice Averaging Group (FLAG) [49].) Our results have a ~10% larger value for the decay constants f_B and f_{B_s} compared to other works at the physical b-quark mass point, which would be plausibly understood as coming from the static approximation ambiguity. The ETM Collaboration's results in the static limit in Ref. [50] also show this tendency. However, the ALPHA Collaboration's results for f_B and f_{B_s} in the static limit indicate a much smaller deviation from those at the physical b-quark mass point [12]. We cannot determine the reason for this difference compared to our results, because our current uncertainty is still large. On the other hand, there is no clear difference from the physical b-quark point in $f_B\sqrt{\hat{B}_B}$, $f_{B_s}\sqrt{\hat{B}_{B_s}}$, $\hat{B}_B$, and $\hat{B}_{B_s}$, because of the large error. For the SU(3)-breaking ratios, a significant deviation from others is not seen since the static approximation uncertainty is largely reduced by the SU(3) light flavor symmetry factor, as described in Eq. (156).

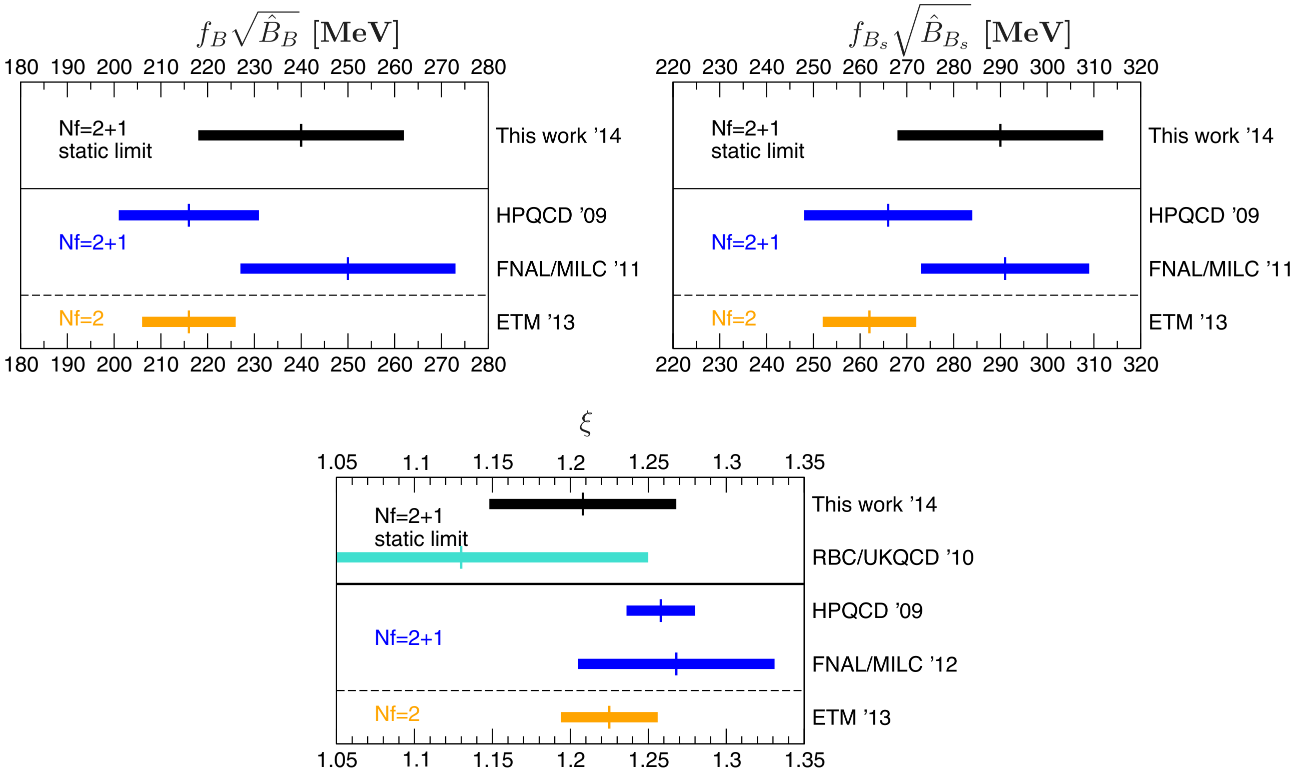

FIG. 8 (color online). Comparison of $f_B\sqrt{\hat{B}_B}$, $f_{B_s}\sqrt{\hat{B}_{B_s}}$, and ξ with other works. The data is cited from Refs. [57] (HPQCD 2009), [58] (FNAL/MILC 2011), [59] (FNAL/MILC 2012), [14] (ETM 2013), and [40] (RBC/UKQCD 2010). The RGI values of $f_B\sqrt{\hat{B}_B}$ and $f_{B_s}\sqrt{\hat{B}_{B_s}}$ in FNAL/MILC 2011 are obtained by converting $f_B\sqrt{B_B}$ and $f_{B_s}\sqrt{B_{B_s}}$ at $\mu = m_b$ in Ref. [58] with the two-loop multiplicative factor 1.516. Errors for the static-limit results do not contain the $1/m_b$ uncertainty.

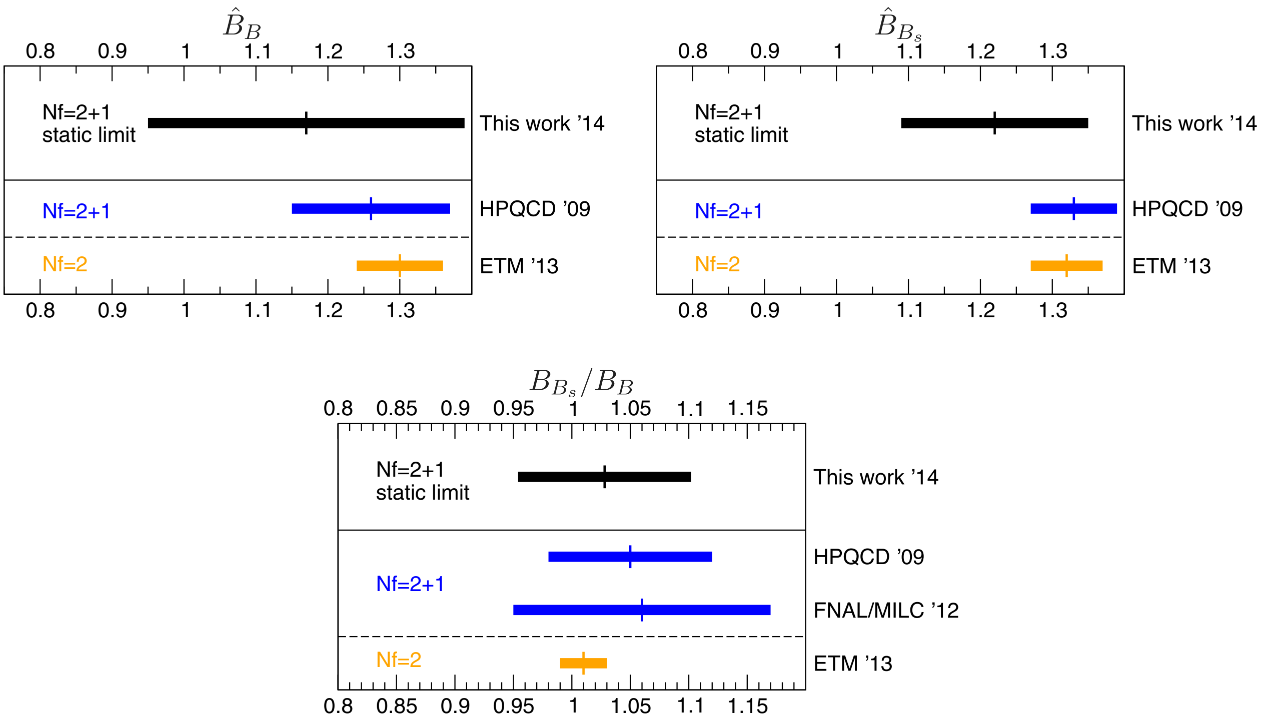

FIG. 9 (color online). Comparison of $\hat{B}_B$, $\hat{B}_{B_s}$, and B_{B_s}/B_B with other works. The data is cited from Refs. [57] (HPQCD 2009), [14] (ETM 2013), and [59] (FNAL/MILC 2012). Errors for the static-limit results do not contain the $1/m_b$ uncertainty.

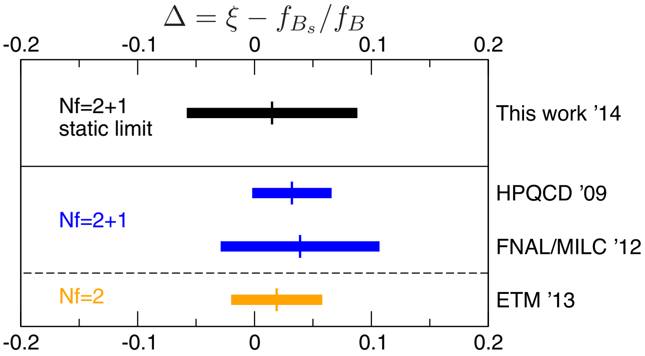

FIG. 10 (color online). Comparison of $\Delta = \xi - f_{B_s}/f_B$ with other works. The data is cited from Refs. [57] (HPQCD 2009), [59] (FNAL/MILC 2012), and [14] (ETM 2013). In calculating Δ, correlations between ξ and f_{B_s}/f_B are not taken into account.

Finally, it would be interesting to see a correspondence between ξ and f_{B_s}/f_B. In this study we obtained the difference

$$\Delta = \xi - \frac{f_{B_s}}{f_B} = 0.015(73), \qquad (157)$$

where the correlation between ξ and f_{B_s}/f_B is omitted. As mentioned in Sec. III A, a naive factorization suggests that ξ is close to f_{B_s}/f_B, and our result supports this observation in the static limit of the b quark. In Fig. 10 we show Δ from other works together with our results. No discrepancy between ξ and f_{B_s}/f_B beyond 1σ error has yet been seen.

C. Further improvements for the next step

Although the obtained results in this work are encouraging, there exist limitations due to insufficient statistics and various systematic errors. As the current error budget in Fig. 6 shows, dominant uncertainties are the statistical error, chiral extrapolation, and the uncertainty from renormalization. To overcome the current situation, we present the following possible options.

All-mode averaging (AMA): Currently, our results have a large statistical error and the chiral extrapolation is suffering from a lack of statistics. Gluon link smearings in the static action help to improve signal qualities to some extent; however, the statistical error is not small enough. The AMA technique [60] provides a substantial computational cost reduction, which leads to improved statistics. In the AMA, a bunch of source points are used to increase statistics while keeping the computational cost small by using a conjugate gradient (CG) solver with relaxed convergence conditions.

Physical light-quark mass point simulation: The lightest pion mass in this paper is ~290 [MeV], which leaves a large uncertainty from the chiral extrapolation. This error would be significantly reduced by a physical point simulation, where the simulated pion mass is ~135 [MeV]. The $2+1$-flavor dynamical ensembles are being generated by the RBC and UKQCD collaborations using Möbius DWF [61], which keeps almost the same lattice spacings as those in this work but with a doubled physical volume [62]. It would increase the computational cost by a large amount, and hence the AMA technique mentioned above is crucial.

Nonperturbative renormalization: While the one-loop renormalization uncertainty is 0% or quite small for the SU(3)-breaking ratios, it is estimated to be at the most 6% for non-ratio quantities. Nonperturbative renormalization is, hence, required for the non-ratio quantities in order to reduce the large uncertainty. The renormalization would be accomplished using the momentum-subtraction (RI/MOM) scheme [63,64], in which an additional renormalization condition is required to manage the $1/a$ power divergence.

These programs are nontrivial but promising directions. Some of them are currently on-going [65] and we plan to present more definite results on this project in the near future.

ACKNOWLEDGMENTS

We thank members of the RBC and UKQCD collaborations, especially Oliver Witzel for useful discussions. The calculations reported here were performed on the QCDOC computers of RIKEN-BNL Research Center and the USQCD Collaboration at Brookhaven National Laboratory (BNL), the RIKEN Integrated Cluster of Clusters (RICC) at RIKEN, Wako, the KMI computer φ at Nagoya University, and resources provided by the USQCD Collaboration funded by the U.S. Department of Energy. The software used includes the CPS QCD codes (http://qcdoc.phys.columbia.edu/cps.html), supported in part by the U.S. DOE SciDAC program. This work is supported in part by JSPS Kakenhi Grants No. 21540289 and 22224003 (Y. A.). T. I., C. L., and A. S. were supported in part by U.S. DOE Contract No. DE-AC02-98CH10886 and T. I. was also supported by JSPS Grants No. 22540301, 23105715 and 26400261.

APPENDIX A: EFFECTIVE MASS AND CORRELATOR PLOTS

Figures 11–15 show effective mass plots in the two-point function and three-point function plots. The fit ranges and fit results are included in the figures.

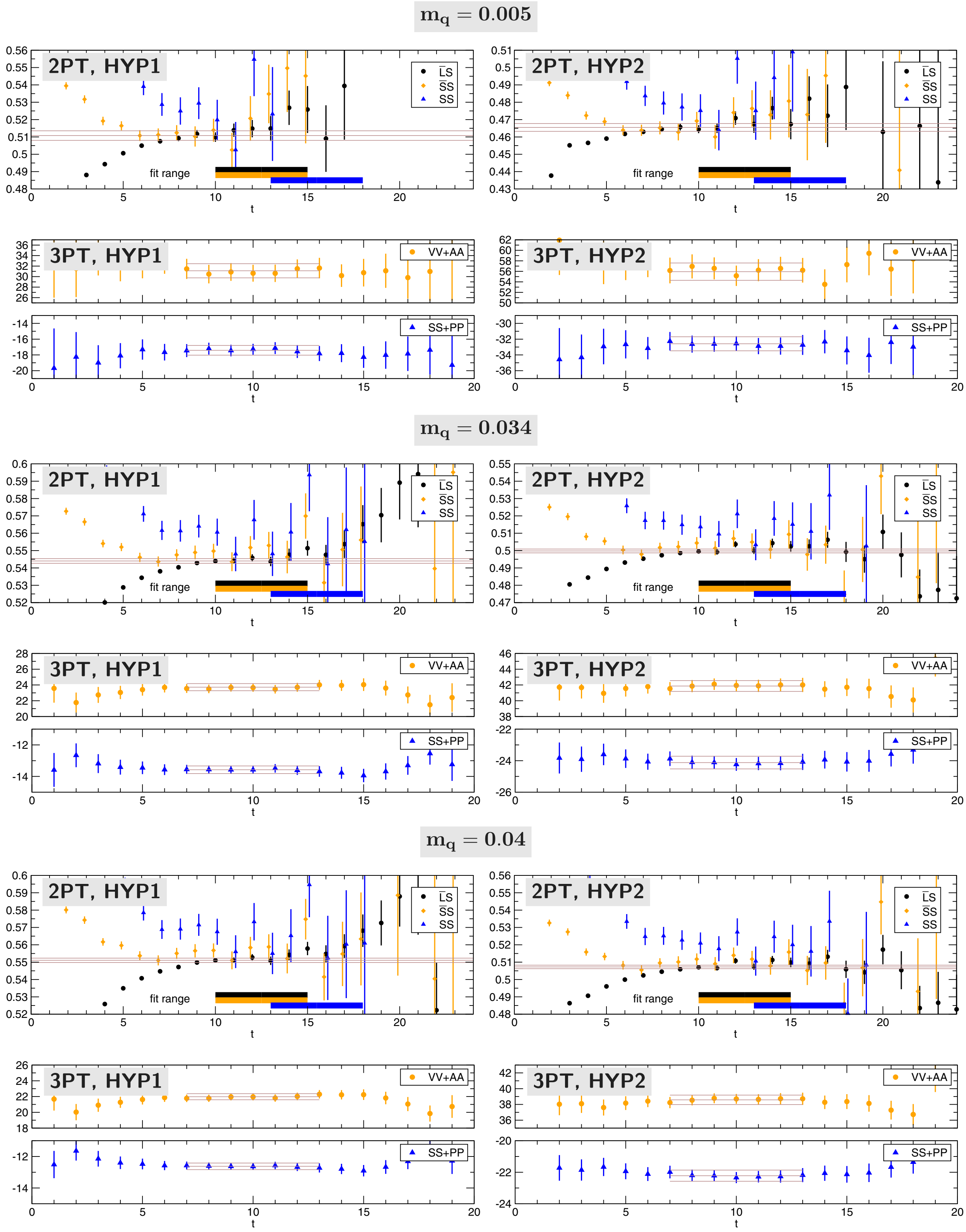

FIG. 11 (color online). Effective mass (two-point function) and three-point function plot for 24c1. The figures show $E_{\rm eff} = -\ln(C^{\rm XX}(t+1,0)/C^{\rm XX}(t,0))$ with XX $= (\tilde{L}S, \tilde{S}S, SS)$ for 2PT, $C_L^{SS}(t_f,t,0)$ for 3PT VV + AA, and $C_S^{SS}(t_f,t,0)$ for 3PT SS + PP. Fit ranges and fit results are shown in the figures. For the three-point functions t_f is fixed to be 20.

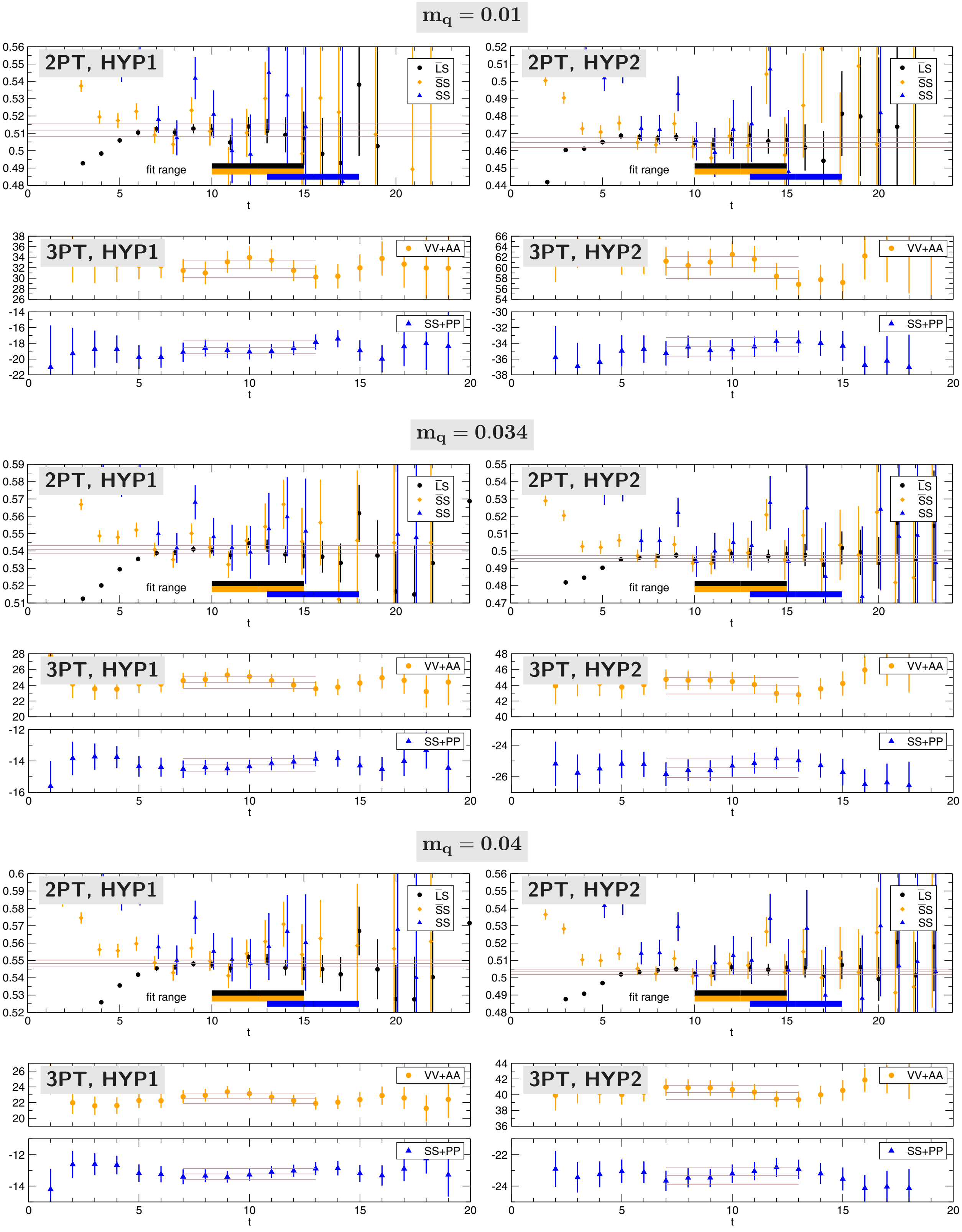

FIG. 12 (color online). Effective mass (two-point function) and three-point function plot for 24c2. The figures show $E_{\mathrm{eff}} = -\ln(C^{\mathrm{XX}}(t+1,0)/C^{\mathrm{XX}}(t,0))$ with XX $= (\tilde{L}S, \tilde{S}S, SS)$ for 2PT, $C_L^{SS}(t_f,t,0)$ for 3PT VV + AA, and $C_S^{SS}(t_f,t,0)$ for 3PT SS + PP. Fit ranges and fit results are shown in the figures. For the three-point functions t_f is fixed to be 20.

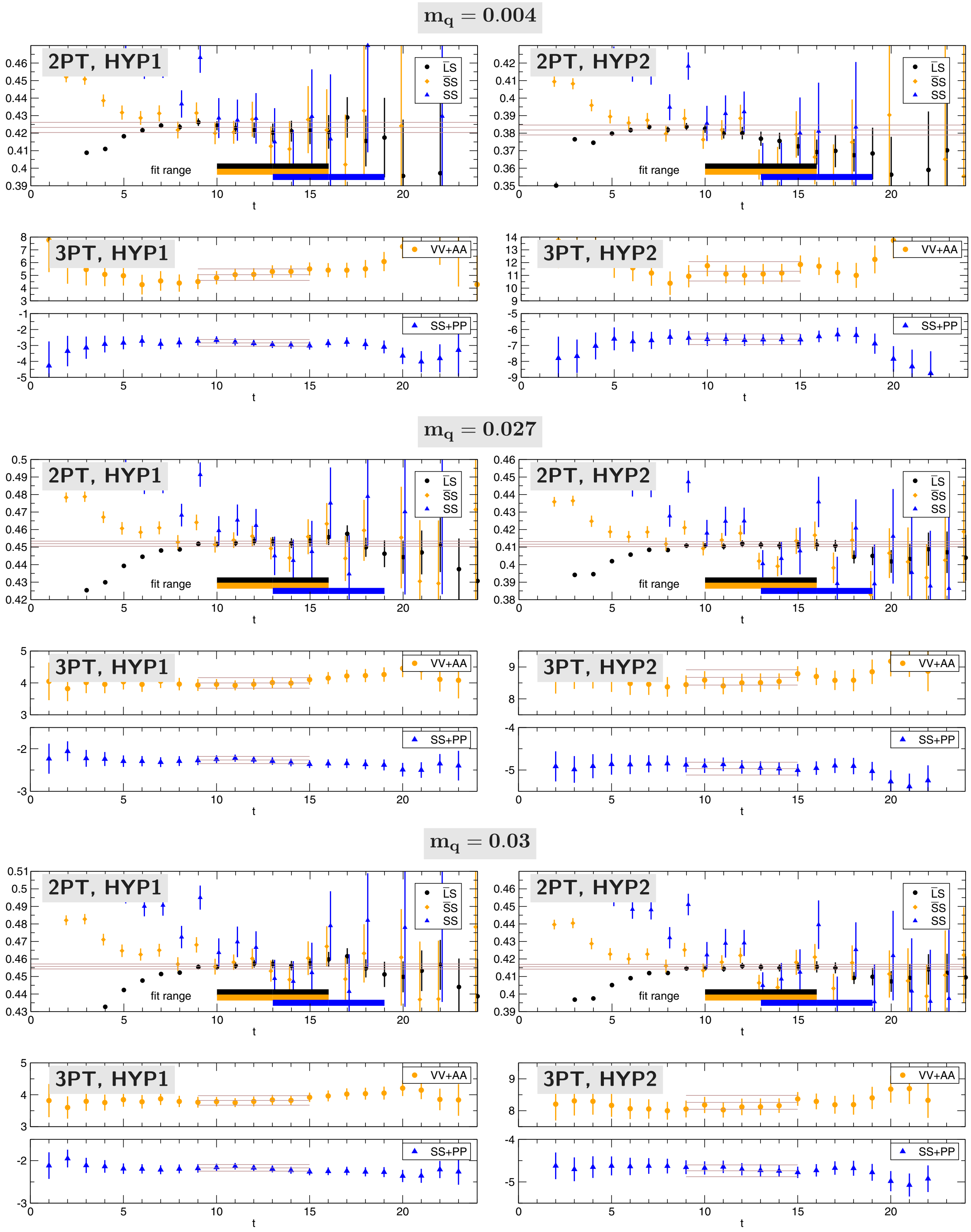

FIG. 13 (color online). Effective mass (two-point function) and three-point function plot for 32c1. The figures show $E_{\rm eff} = -\ln(C^{\rm XX}(t+1,0)/C^{\rm XX}(t,0))$ with XX = $(\tilde{L}S, \tilde{S}S, SS)$ for 2PT, $C_L^{SS}(t_f,t,0)$ for 3PT VV + AA, and $C_S^{SS}(t_f,t,0)$ for 3PT SS + PP. Fit ranges and fit results are shown in the figures. For the three-point functions t_f is fixed to be 24.

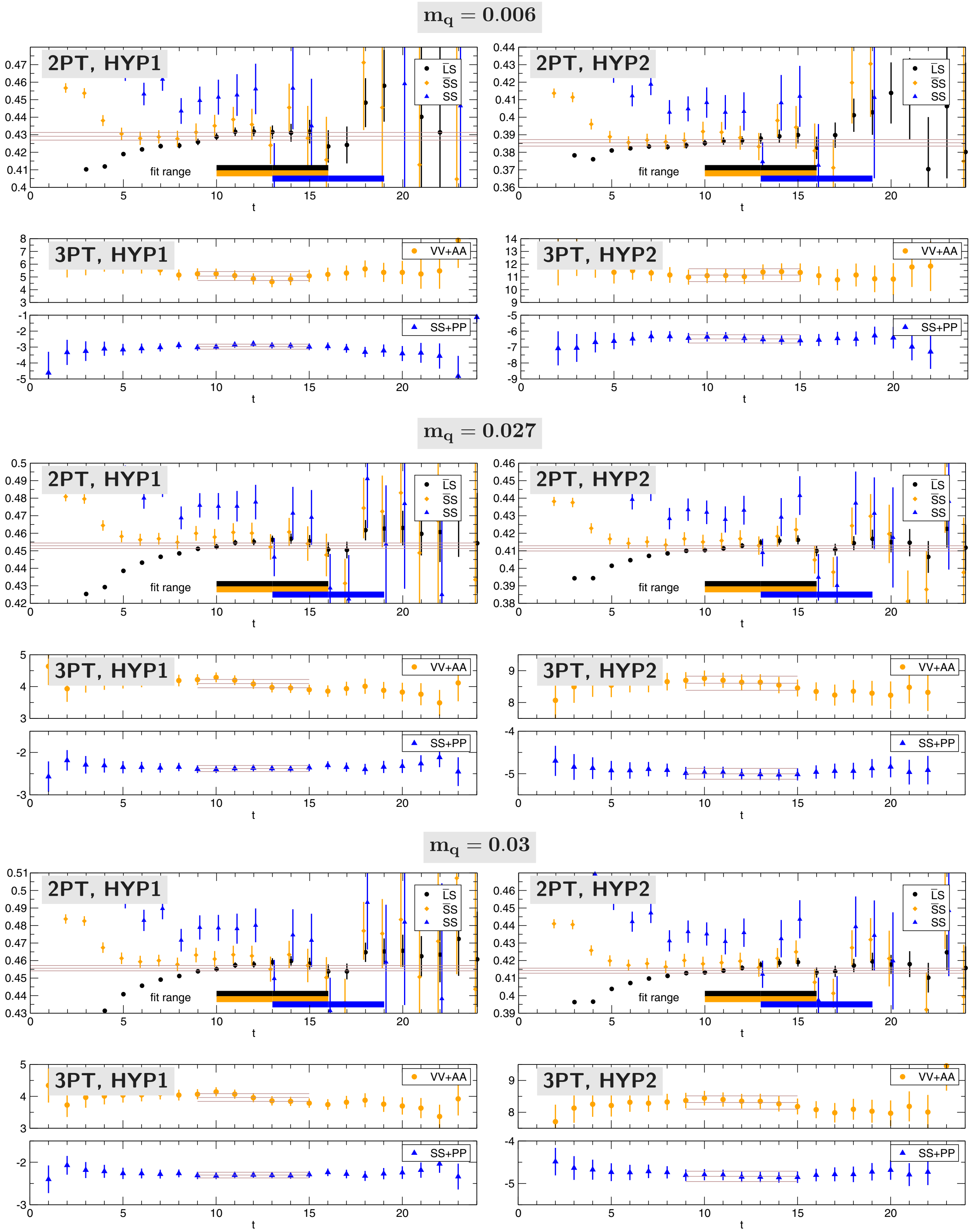

FIG. 14 (color online). Effective mass (two-point function) and three-point function plot for 32c2. The figures show $E_{\mathrm{eff}} = -\ln(C^{\mathrm{XX}}(t+1,0)/C^{\mathrm{XX}}(t,0))$ with XX $= (\tilde{L}S, \tilde{S}S, SS)$ for 2PT, $C_L^{SS}(t_f,t,0)$ for 3PT VV + AA, and $C_S^{SS}(t_f,t,0)$ for 3PT SS + PP. Fit ranges and fit results are shown in the figures. For the three-point functions t_f is fixed to be 24.

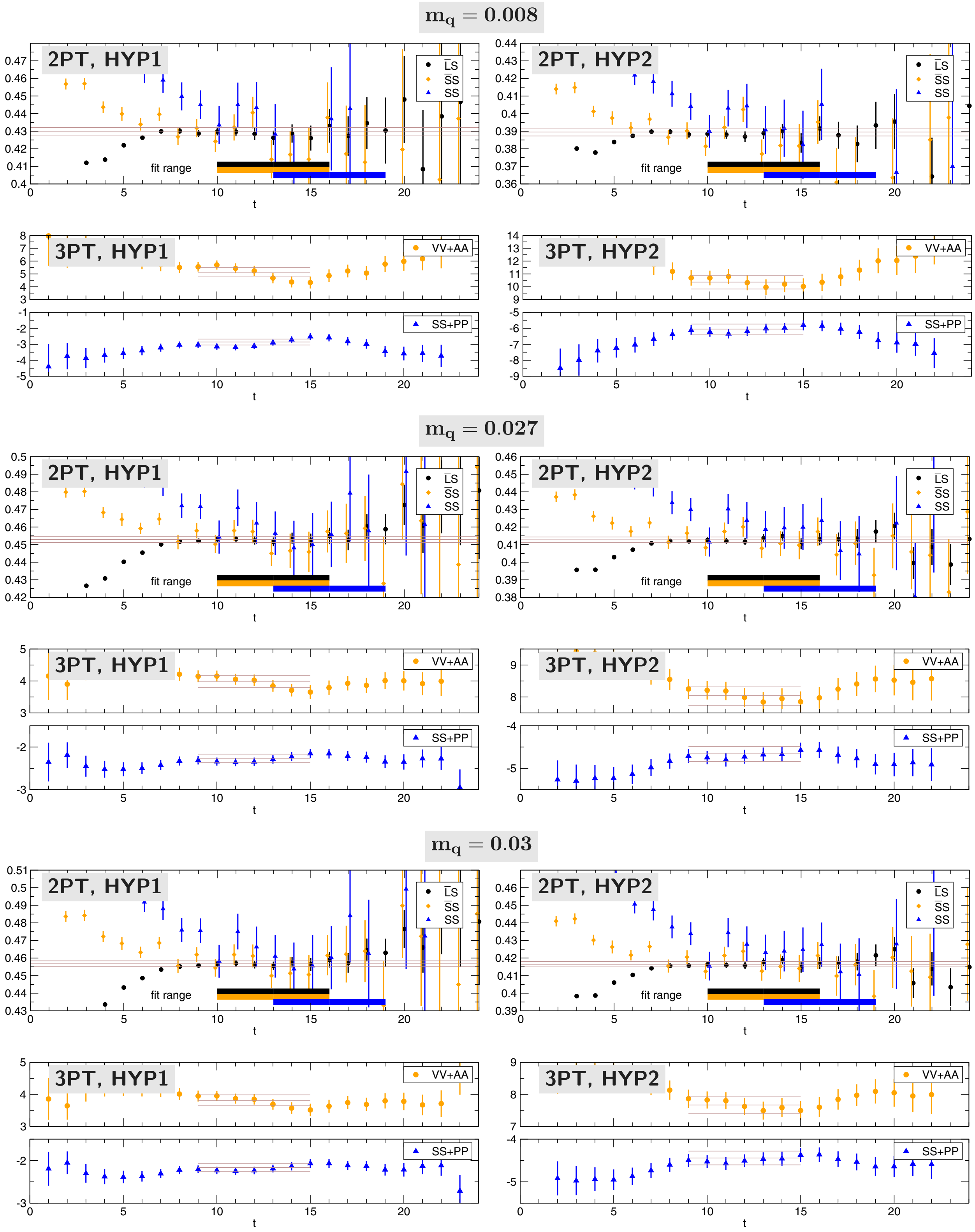

FIG. 15 (color online). Effective mass (two-point function) and three-point function plot for 32c3. The figures show $E_{\rm eff} = -\ln(C^{XX}(t+1,0)/C^{XX}(t,0))$ with XX $= (\tilde{L}S, \tilde{S}S, SS)$ for 2PT, $C_L^{SS}(t_f,t,0)$ for 3PT VV + AA, and $C_S^{SS}(t_f,t,0)$ for 3PT SS + PP. Fit ranges and fit results are shown in the figures. For the three-point functions t_f is fixed to be 24.

APPENDIX B: FIT-RANGE DEPENDENCE

We show the fit range dependencies of physical quantities at each simulation point in Figs. 16,17, and 18. To check the dependencies, we shift the minimal value of t in the fit range toward a larger value by 2 for the 2PT functions and shorten the range by 2 for the 3PT functions, which we name “fit range 2” in the figures. To be more specific, the actual fit ranges are

$$\begin{aligned}
\text{original (24c)}:\ & t=10\text{–}15\ (\bar{\mathrm{L}}\mathrm{S},\bar{\mathrm{S}}\mathrm{S}),\quad t=13\text{–}18\ (\mathrm{SS}),\\
& t=7\text{–}13\ (\mathrm{VV}+\mathrm{AA},\mathrm{SS}+\mathrm{PP}),\\
\text{original (32c)}:\ & t=10\text{–}16\ (\bar{\mathrm{L}}\mathrm{S},\bar{\mathrm{S}}\mathrm{S}),\quad t=13\text{–}19\ (\mathrm{SS}),\\
& t=9\text{–}15\ (\mathrm{VV}+\mathrm{AA},\mathrm{SS}+\mathrm{PP}),\\
\text{fit range 2 (24c)}:\ & t=12\text{–}15\ (\bar{\mathrm{L}}\mathrm{S},\bar{\mathrm{S}}\mathrm{S}),\quad t=15\text{–}18\ (\mathrm{SS}),\\
& t=8\text{–}12\ (\mathrm{VV}+\mathrm{AA},\mathrm{SS}+\mathrm{PP}),\\
\text{fit range 2 (32c)}:\ & t=12\text{–}16\ (\bar{\mathrm{L}}\mathrm{S},\bar{\mathrm{S}}\mathrm{S}),\quad t=15\text{–}19\ (\mathrm{SS}),\\
& t=10\text{–}14\ (\mathrm{VV}+\mathrm{AA},\mathrm{SS}+\mathrm{PP}).
\end{aligned}$$

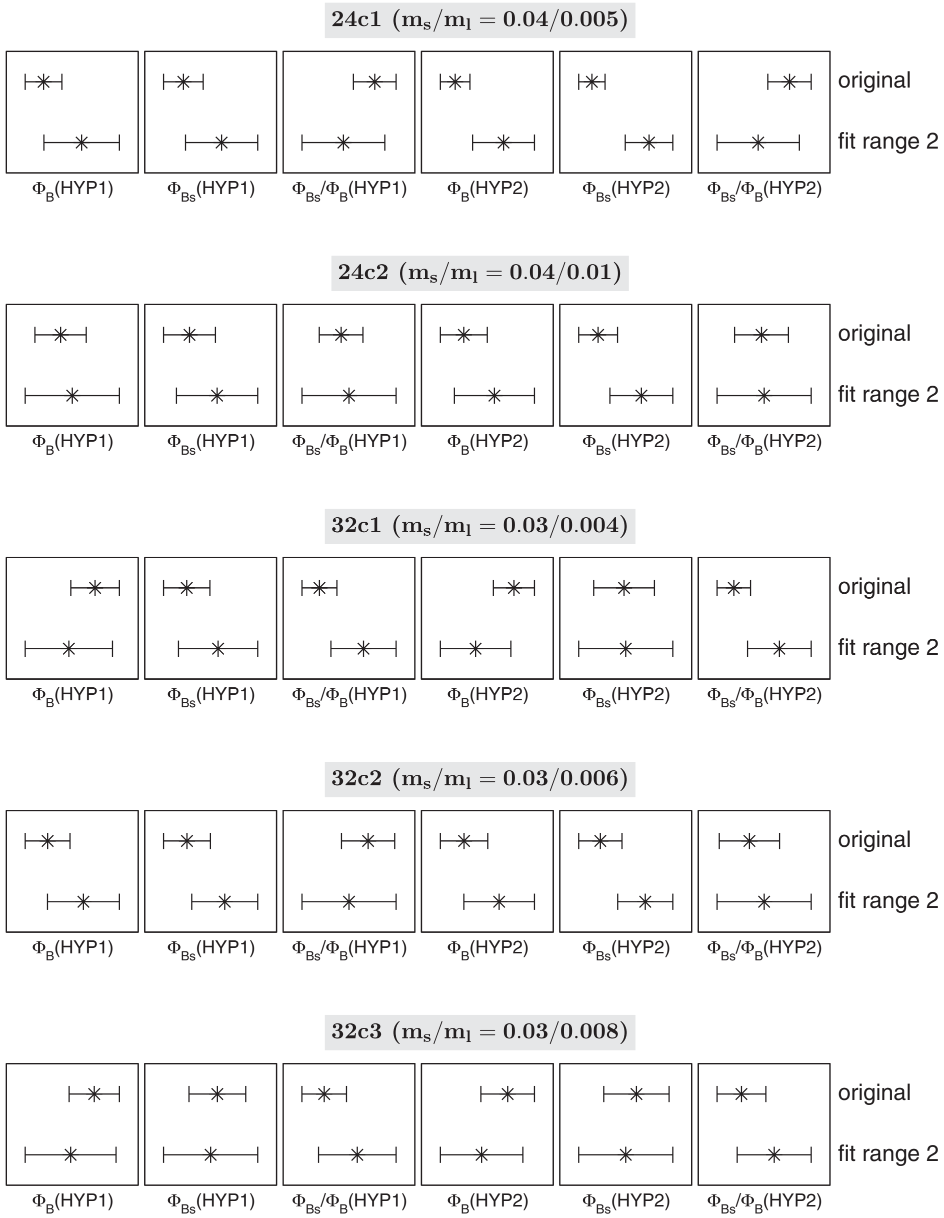

FIG. 16. Fit-range dependencies of Φ_B, Φ_{B_s}, and Φ_{B_s}/Φ_B at each simulation point. Horizontal labels are suppressed. We find differences between the fit-range choices beyond 1σ statistical error in 24c1(Φ_B, Φ_{B_s}), 24c2(Φ_{B_s}), 32c1(Φ_B, Φ_{B_s}/Φ_B), and 32c2(Φ_{B_s}).

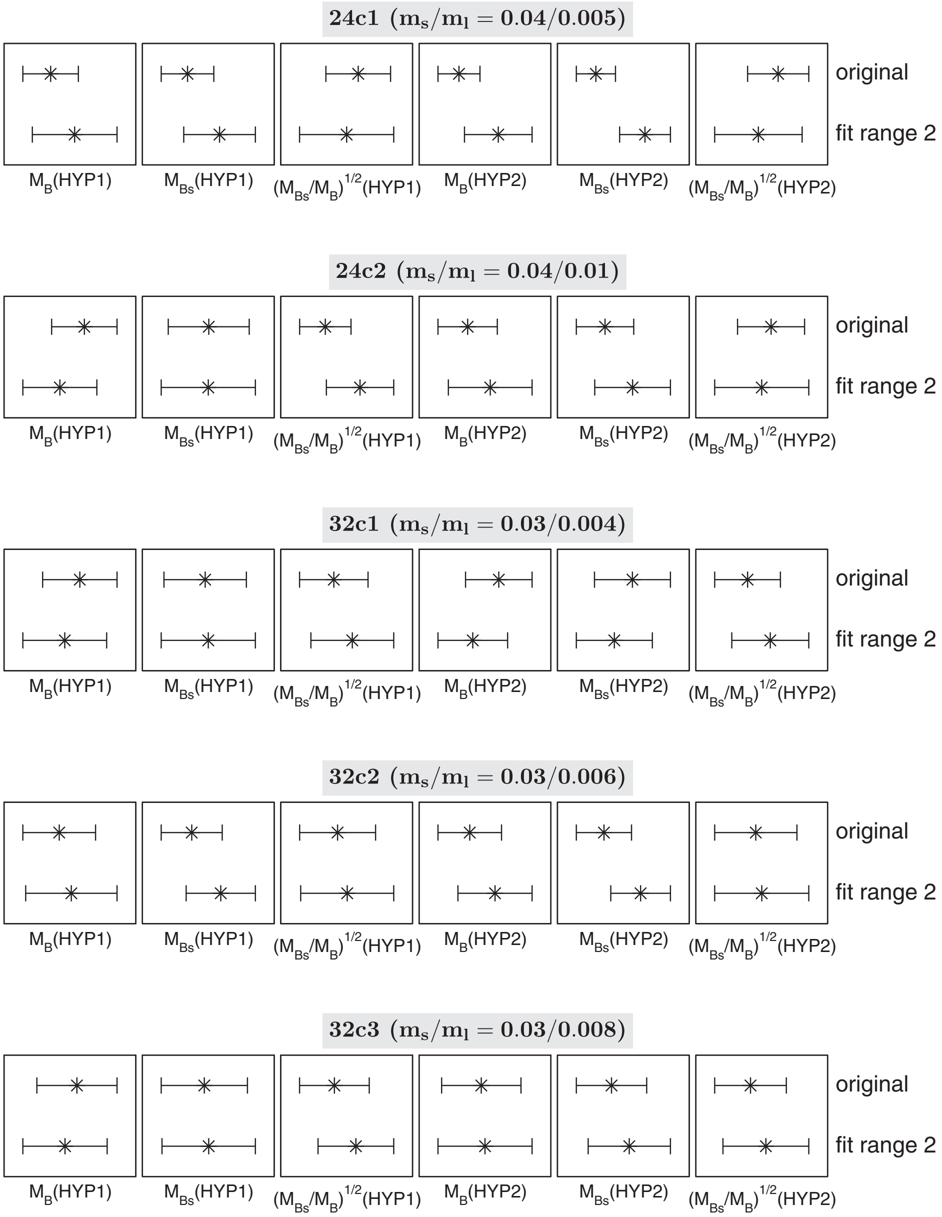

FIG. 17. Fit-range dependencies of M_B, M_{B_s}, and $(M_{B_s}/M_B)^{1/2}$ at each simulation point. Horizontal labels are suppressed. We find differences between the fit-range choices beyond 1σ statistical error in 24c1(M_B, M_{B_s}), 24c2($(M_{B_s}/M_B)^{1/2}$), and 32c2(M_{B_s}).

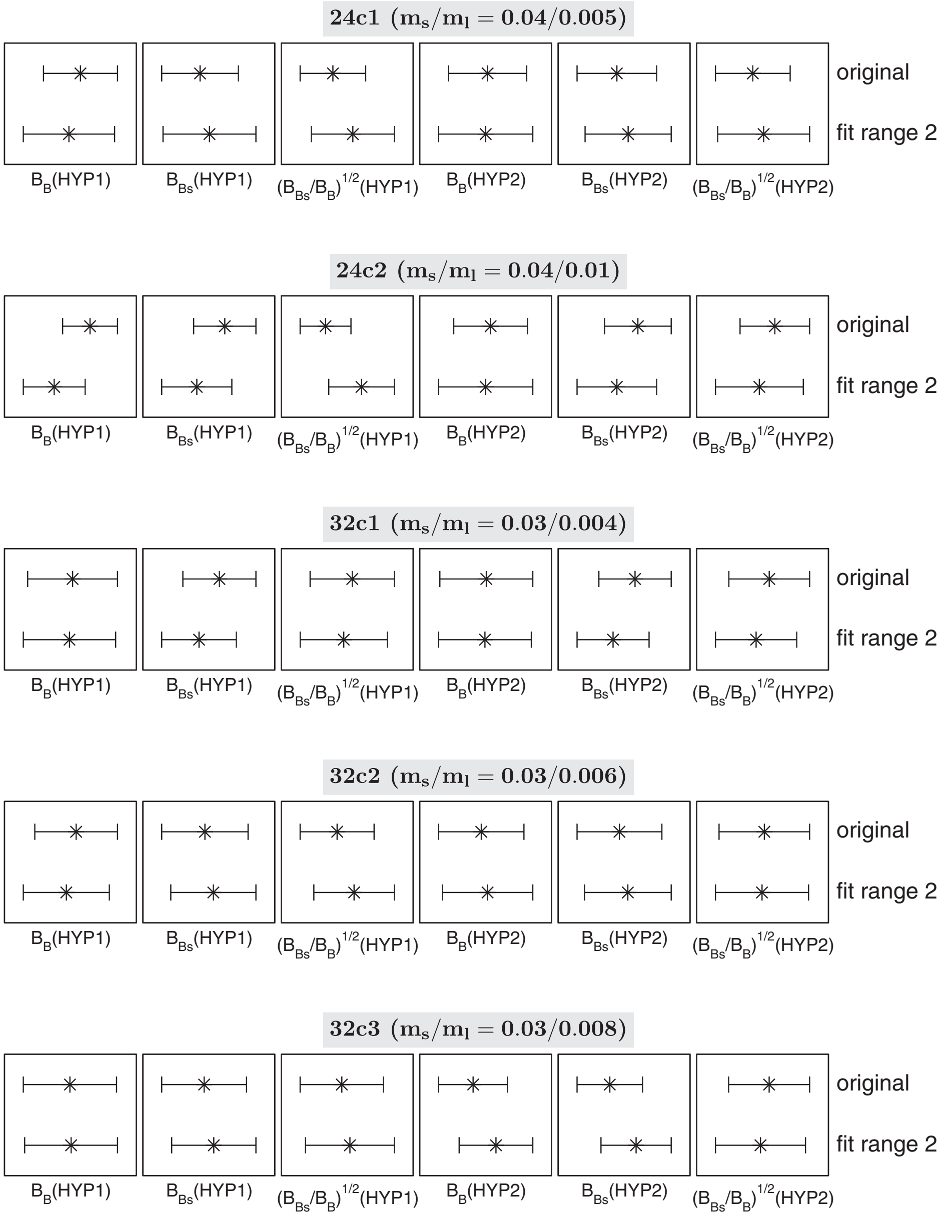

FIG. 18. Fit-range dependencies of B_B, B_{B_s}, and $(B_{B_s}/B_B)^{1/2}$ at each simulation point. Horizontal labels are suppressed. We find differences between the fit-range choices beyond 1σ statistical error in 24c2(B_B, $(B_{B_s}/B_B)^{1/2}$).

We find disagreements between the choices of the fit ranges beyond 1σ statistical error for some cases.

[1] M. Kobayashi and T. Maskawa, Prog. Theor. Phys. **49**, 652 (1973).

[2] T. Inami and C. S. Lim, Prog. Theor. Phys. **65**, 297 (1981); **65**, 1772(E) (1981).

[3] C. W. Bernard, T. Blum, and A. Soni, Phys. Rev. D **58**, 014501 (1998).

[4] E. Eichten and B. R. Hill, Phys. Lett. B **234**, 511 (1990).

[5] E. Eichten and B. R. Hill, Phys. Lett. B **240**, 193 (1990).

[6] G. P. Lepage, Nucl. Phys. B, Proc. Suppl. **26**, 45 (1992).

[7] M. Della Morte, S. Dürr, J. Heitger, H. Molke, J. Rolf, A. Shindler, and R. Sommer (ALPHA Collaboration), Phys. Lett. B **581**, 93 (2004); **612**, 313(E) (2005).

[8] M. Della Morte, A. Shindler, and R. Sommer, J. High Energy Phys. 08 (2005) 051.
[9] J. Heitger, and R. Sommer (ALPHA Collaboration), J. High Energy Phys. 02 (2004) 022.
[10] L. Maiani, G. Martinelli, and C. T. Sachrajda, Nucl. Phys. **B368**, 281 (1992).
[11] C. W. Bernard, J. N. Labrenz, and A. Soni, Phys. Rev. D **49**, 2536 (1994).
[12] F. Bernardoni *et al.*, Phys. Lett. B **735**, 349 (2014).
[13] B. Blossier *et al.* (ETM Collaboration), J. High Energy Phys. 04 (2010) 049.
[14] N. Carrasco *et al.* (ETM Collaboration), J. High Energy Phys. 03 (2014) 016.
[15] J. Beringer *et al.* (Particle Data Group), Phys. Rev. D **86**, 010001 (2012).
[16] A. J. Buras, M. Jamin, and P. H. Weisz, Nucl. Phys. **B347**, 491 (1990).
[17] K. G. Chetyrkin, Phys. Lett. B **404**, 161 (1997).
[18] J. A. M. Vermaseren, S. A. Larin, and T. van Ritbergen, Phys. Lett. B **405**, 327 (1997).
[19] A. Hasenfratz and F. Knechtli, Phys. Rev. D **64**, 034504 (2001).
[20] D. B. Kaplan, Phys. Lett. B **288**, 342 (1992).
[21] R. Narayanan and H. Neuberger, Phys. Lett. B **302**, 62 (1993).
[22] Y. Shamir, Nucl. Phys. **B406**, 90 (1993).
[23] J. Noaki and Y. Taniguchi, Phys. Rev. D **61**, 054505 (2000).
[24] Y. Iwasaki, Nucl. Phys. **B258**, 141 (1985).
[25] Y. Iwasaki, arXiv:1111.7054.
[26] Y. Aoki *et al.* (RBC and UKQCD Collaborations), Phys. Rev. D **83**, 074508 (2011).
[27] A. J. Buras and P. H. Weisz, Nucl. Phys. **B333** (1990) 66.
[28] J. M. Flynn, O. F. Hernandez, and B. R. Hill, Phys. Rev. D **43**, 3709 (1991).
[29] G. Buchalla, Phys. Lett. B **395**, 364 (1997).
[30] T. Ishikawa, Y. Aoki, J. M. Flynn, T. Izubuchi, and O. Loktik, J. High Energy Phys. 05 (2011) 040.
[31] X. D. Ji and M. J. Musolf, Phys. Lett. B **257**, 409 (1991).
[32] D. J. Broadhurst and A. G. Grozin, Phys. Lett. B **267**, 105 (1991).
[33] V. Gimenez, Nucl. Phys. **B401**, 116 (1993).
[34] M. Ciuchini, E. Franco, and V. Gimenez, Phys. Lett. B **388**, 167 (1996).
[35] D. Becirevic and J. Reyes, Nucl. Phys. B, Proc. Suppl. **129–130**, 435 (2004).
[36] B. Blossier, Phys. Rev. D **76**, 114513 (2007).
[37] M. Papinutto, G. Herdoiza, C. Pena, and A. Vladikas, *Proc. Sci.*, LATTICE2013 (2013) 317 [arXiv:1311.5177].
[38] G. P. Lepage and P. B. Mackenzie, Phys. Rev. D **48**, 2250 (1993).
[39] N. H. Christ, T. T. Dumitrescu, O. Loktik, and T. Izubuchi, *Proc. Sci.*, LAT2007 (2007) 351 [arXiv:0710.5283].
[40] C. Albertus *et al.*, Phys. Rev. D **82**, 014505 (2010).
[41] C. Alexandrou, S. Gusken, F. Jegerlehner, K. Schilling, and R. Sommer, Nucl. Phys. **B414**, 815 (1994).
[42] F. Berruto, T. Blum, K. Orginos, and A. Soni, Phys. Rev. D **73**, 054509 (2006).
[43] C. Allton *et al.* (RBC-UKQCD Collaboration), Phys. Rev. D **78**, 114509 (2008).
[44] W. Detmold, C.-J. D. Lin, and S. Meinel, Phys. Rev. Lett. **108**, 172003 (2012).
[45] C. Bernard (MILC Collaboration), Phys. Rev. D **65**, 054031 (2002).
[46] G. Colangelo, S. Durr, and C. Haefeli, Nucl. Phys. **B721**, 136 (2005).
[47] D. Arndt and C. J. D. Lin, Phys. Rev. D **70**, 014503 (2004).
[48] C. Aubin and C. Bernard, Phys. Rev. D **73**, 014515 (2006).
[49] S. Aoki *et al.*, Eur. Phys. J. C **74**, 2890 (2014).
[50] P. Dimopoulos *et al.* (ETM Collaboration), J. High Energy Phys. 01 (2012) 046.
[51] R. J. Dowdall, C. T. H. Davies, R. R. Horgan, C. J. Monahan, and J. Shigemitsu (HPQCD Collaboration), Phys. Rev. Lett. **110**, 222003 (2013).
[52] N. Carrasco *et al.*, *Proc. Sci.*, LATTICE2013 (2013) 313 [arXiv:1311.2837].
[53] C. McNeile, C. T. H. Davies, E. Follana, K. Hornbostel, and G. P. Lepage, Phys. Rev. D **85**, 031503 (2012).
[54] H. Na, C. J. Monahan, C. T. H. Davies, R. Horgan, G. P. Lepage, and J. Shigemitsu, Phys. Rev. D **86**, 034506 (2012).
[55] A. Bazavov *et al.* (Fermilab Lattice and MILC Collaborations), Phys. Rev. D **85**, 114506 (2012).
[56] N. H. Christ, J. M. Flynn, T. Izubuchi, T. Kawanai, C. Lehner, A. Soni, R. S. Van de Water, and O. Witzel, Phys. Rev. D **91**, 054502 (2015).
[57] E. Gamiz, C. T. H. Davies, G. P. Lepage, J. Shigemitsu, and M. Wingate (HPQCD Collaboration), Phys. Rev. D **80**, 014503 (2009).
[58] C. M. Bouchard, E. D. Freeland, C. Bernard, A. X. El-Khadra, E. Gamiz, A. S. Kronfeld, J. Laiho, and R. S. Van de Water, *Proc. Sci.*, LATTICE2011 (2011) 274 [arXiv:1112.5642].
[59] A. Bazavov *et al.*, Phys. Rev. D **86**, 034503 (2012).
[60] T. Blum, T. Izubuchi, and E. Shintani, Phys. Rev. D **88**, 094503 (2013).
[61] R. C. Brower, H. Neff, and K. Orginos, Nucl. Phys. B, Proc. Suppl. **140**, 686 (2005).
[62] T. Blum *et al.*, *Proc. Sci.*, LATTICE2013 (2013) 404.
[63] G. Martinelli, S. Petrarca, C. T. Sachrajda, and A. Vladikas, Phys. Lett. B **311**, 241 (1993); **317**, 660(E) (1993).
[64] G. Martinelli, C. Pittori, C. T. Sachrajda, M. Testa, and A. Vladikas, Nucl. Phys. **B445**, 81 (1995).
[65] T. Ishikawa, Y. Aoki, T. Izubuchi, C. Lehner, and A. Soni, *Proc. Sci.*, LATTICE2013 (2013) 410 [arXiv:1312.1010].